



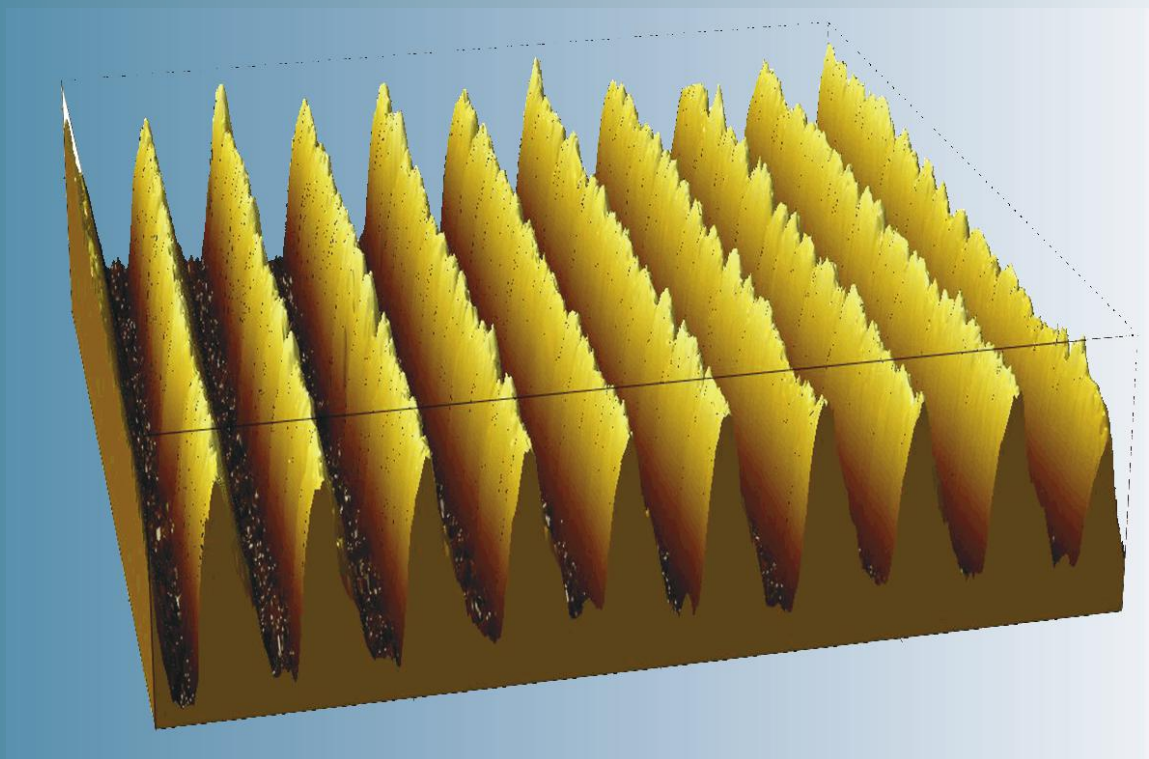
ISSN 1028-8546

Volume XX, Number 2
Section: En
July, 2014

Azerbaijan Journal of Physics

Fizika

www.physics.gov.az



G.M. Abdullayev Institute of Physics
Azerbaijan National Academy of Sciences
Department of Physical, Mathematical and Technical Sciences

Published from 1995
Ministry of Press and Information
of Azerbaijan Republic,
Registration number 402, 16.04.1997

ISSN 1028-8546
vol. XX, Number 2, 2014
Series: En

Azerbaijan Journal of Physics

FIZIKA

*G.M.Abdullayev Institute of Physics
Azerbaijan National Academy of Sciences
Department of Physical, Mathematical and Technical Sciences*

HONORARY EDITORS

Arif PASHAYEV

EDITORS-IN-CHIEF

Nazim MAMEDOV

Chingiz QAJAR

SENIOR EDITOR

Talat MEHDIYEV

INTERNATIONAL REVIEW BOARD

Ivan Scherbakov, Russia
Kerim Allahverdiyev, Azerbaijan
Mehmet Öndr Yetiş, Turkey
Gennadii Jablonskii, Buelorussia
Rafael Imamov, Russia
Vladimir Man'ko, Russia
Eldar Salayev, Azerbaijan
Dieter Hochheimer, USA
Victor L'vov, Israel
Vyacheslav Tuzlukov, South Korea
Majid Ebrahim-Zadeh, Spain

Firudin Hashimzadeh, Azerbaijan
Anatoly Boreysho, Russia
Mikhail Khalin, Russia
Hasan Bidadi, Tebriz, East Azerbaijan, Iran
Natiq Atakishiyev, Mexico
Maksud Aliyev, Azerbaijan
Iskender Djafarov, Azerbaijan
Arif Hashimov, Azerbaijan
Vali Huseynov, Azerbaijan
Javad Abdinov, Azerbaijan
Bagadur Tagiyev, Azerbaijan

Tayar Djafarov, Azerbaijan
Talat Mehdiyev, Azerbaijan
Emil Guseynov, Azerbaijan
Ayaz Baramov, Azerbaijan
Tofiq Mammadov, Azerbaijan
Salima Mehdiyeva, Azerbaijan
Shakir Nagiyev, Azerbaijan
Rauf Guseynov, Azerbaijan
Almuk Abbasov, Azerbaijan
Yusif Asadov, Azerbaijan

TECHNICAL EDITORIAL BOARD

Senior secretary Elmira Akhundova, Nazli Guseynova, Sakina Aliyeva,
Nigar Akhundova, Elshana Aleskerova

PUBLISHING OFFICE

131 H.Javid ave, AZ-1143, Baku
ANAS, G.M.Abdullayev Institute of Physics

Tel.: (99412) 439-51-63, 439-32-23
Fax: (99412) 447-04-56
E-mail: jophphysics@gmail.com
Internet: www.physics.gov.az

It is authorized for printing:

Published at "SƏRQ-QƏRB"
17 Ashug Alessger str., Baku
Typographer : Aziz Gulaliyev

Sent for printing on: ___. 201__
Printing approved on: ___. 201__
Physical binding: _____
Number of copies: ____ 200
Order: _____

THE FREQUENCY DEPENDENCE OF MICROPIXEL AVALANCHE PHOTODIODE CAPACITANCE

E.A. JAFAROVA¹, Z.Y. SADIGOV^{1,2}, F.I. AKHMEDOV³,
A.Z. SADIGOV³, L.A. ALIYEVA¹

¹*Institute of Physics of ANAS mamed by G.M.Abdullayeva, AZ-1143, Baku, Azerbaijan*

²*United Institute of Nuclear Investigations, 141980, Dubna, Russia*

³*Institute of Radiational Problems, AZ-1143, Baku, Azerbaijan*

E-mail: celmira1@rambler.ru

The capacitance properties of silicon micropixel avalanche photodiode at influence of small alternative signal of different frequency ($10\text{ kHz} \div 1\text{ MHz}$). It is shown that at small values of constant voltage applied to the structure, the significant decrease of measured capacitance at the decrease of alternative signal frequency is observed. It is established that decrease of measured capacitance is connected with appearance of series resistance at avalanche photodiode depletion.

Keywords: avalanche photodiode, capacitance of p-n transition, concentration of ionized impurity.

PACS:07.77-n; 07.77.-Ka; 29.40Wk; 85.30De; 85.60Dw

INTRODUCTION

The micropixel avalanche photodiodes (MAPD) developed last time and having the high amplification coefficient $\sim 10^5$, able to register the unit light quanta with high efficiency (40%), have the wide application to prepare devices and equipment for scientific investigations, in particular, in medical and nuclear physical equipment and also for radiation control [1-3].

The principle of operation and production technique of the investigated samples MAPD with deeply put pixels are described in detail in [4,5]. The samples are produced towards with Zecotek Imaging Singapore firm. In these photodiodes the potential distribution in depletion region of epitaxial layers has the peculiarities that it causes by the presence of high-doped matrix from n^+ -regions between two epitaxial layers of p-type conduction [6]. Earlier the capacitance properties of analogous samples are investigated at the only frequency 10MHz [7]. However, the investigation of the dependence of MAPD

structure barrier capacitance on alternative signal frequency is of the interest.

MEASUREMENT TECHNIQUE

The installation scheme for capacitance measurement of investigated diodes is presented in fig.1. The sinusoidal electric signal with constant amplitude 40mB is fed to the sample by generator Textronix AFG3102. Frequency f of alternative signal is varied in limits from 10kHz up to 1MHz. Taking under consideration the properties of differentiating chain, the resistance R_3 is chosen so that signal amplitude, taken on him (oscilloscope indications DP07254) would be not above 250mV. Moreover, measurement accuracy of capacitance is 7%. For example, $R_3 = 1\text{k}\Omega\text{m}$ is chosen for frequency 10kHz; $R_3 = 257\text{Om}$ for 30 kHz; $R_3 = 60\text{Om}$ for 100 kHz; $R_3 = 30\text{Om}$ for 600 kHz and $R_3 = 11.3\text{Om}$ for 1MHz.

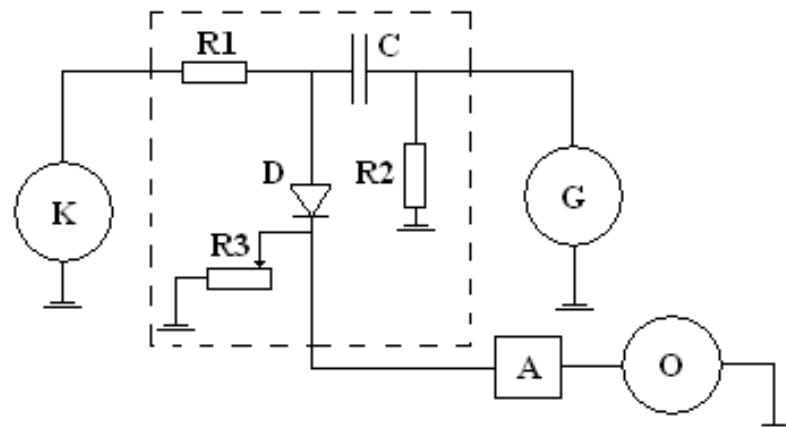


Fig.1. Electrical scheme of capacitance measurement of micropixel avalanche photodiodes: **K** is power supply (Keithley 6487), **G** is generator (Textronix AFG310), **A** is amplifier and **O** is oscilloscope (HANTEK DP07254).

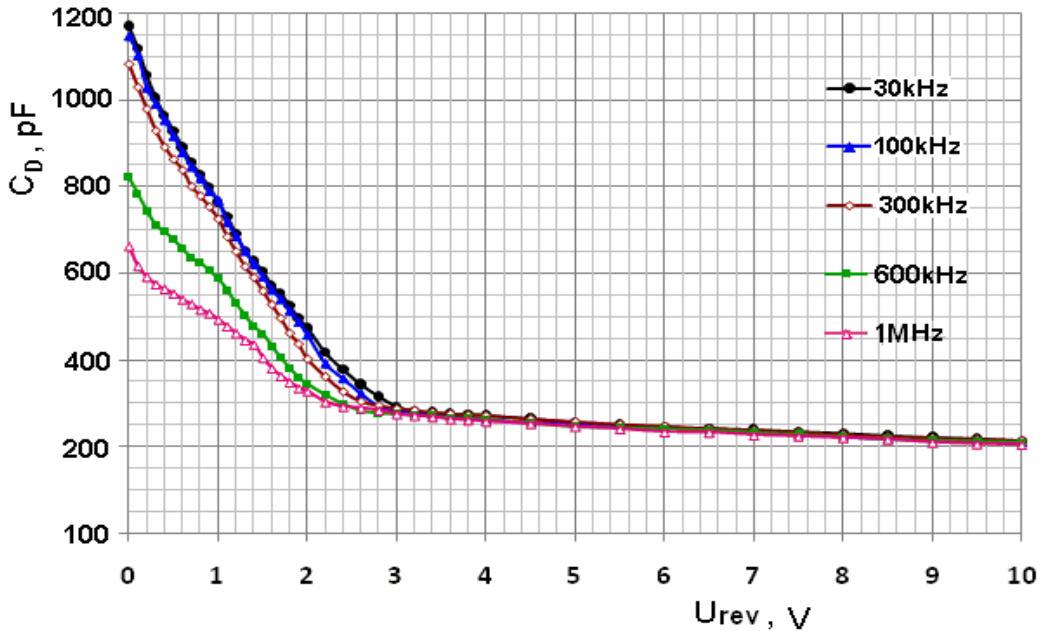


Fig.2 The dependence of photodiode capacitance MAPD-3N on applied voltage at different frequencies f .

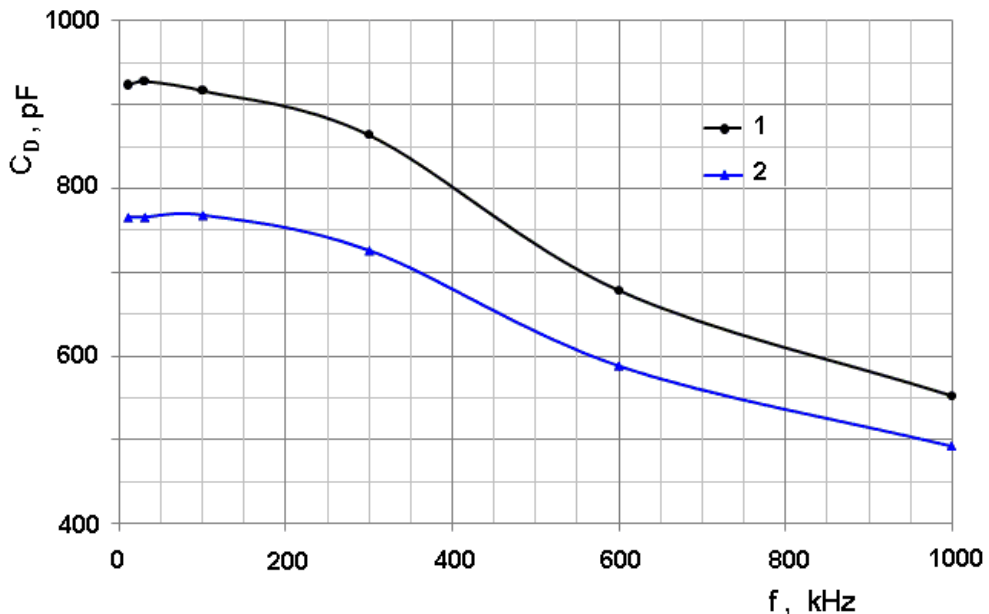


Fig.3. The frequency dependence of measurement capacitance at two fixed value of applied voltage: 1 is $U_{rev}=0.5V$; 2 is $U_{rev}=1V$.

The previous calibration of measurement equipment is carried out with the help of etalon high-frequency condensers with capacitances 220 and 440 pF. They are connected into scheme instead of diode under consideration and the corresponding voltage drop U_{et} is obtained. For measurement of C_D photodiode capacitance accuracy in interval $U_{rev} = (0 \div 2)V$ is chosen the calibration capacitance $C_{et}=440$ pF, and $C_{et}=220$ pF is chosen in interval $U_{rev} = (2 \div 20)V$.

MAPD of "MAPD-3N" type having the operating voltage $U_{op,v}=90.2V$ is chosen in the capacitance of investigated sample. Voltage drop U_D on load R_3 is fixed if power supply Keithley 6487(K) gives constant voltage on the sample. The avalanche photodiode capacitance is defined by the following relation: $C_D = \frac{U_D}{U_{ET}} C_{ET}$.

RESULTS AND THEIR DISCUSSION

The measurements results of barrier capacitance of "MAPD-3N" photodiode in the dependence on applied voltage at different frequencies f of alternative signal are presented in fig. 2. At low values of $U_{rev}=0 \div 3V$ voltage the measurement capacitance strongly depends on alternative signal frequency. The dependence of capacitance on frequency significantly slows down and becomes almost insignificant one after 5V with the growth of applied voltage U_{rev} .

The dependence of capacitance on frequency in small voltages ($0 \div 5V$) region is connected with construction peculiarity of investigated sample MAPD. The presence of matrix from $n+$ -regions between two

epitaxial layers of p-type conduction leads to appearance of some effective between epitaxial layers.

As the depleted layer begins on substrate boundary with first epitaxial layer, then above mentioned effective resistance behaves itself as series connected one with measurement capacitance. Indeed, the influence of this resistance on measurement capacitance will depend on alternative signal frequency: the higher frequency the stronger this influence, that is confirmed by results represented in fig. 3. As it is seen from fig. 3, the device capacitance in $10\text{--}100\text{kHz}$ frequency region practically remains constant. This evidences about the fact that photodiode reactive resistance is significantly bigger than

value of series resistance and that's why the measurement capacitance is equal to device barrier capacitance.

CONCLUSION

It is shown that MAPD measurement capacitance with deeply put pixels depends on frequency of small alternative signal superimposed on constant voltage. The strongest frequency dependence is observed in constant shifting region $U_{rev}=0\text{--}3\text{V}$. It is established that for correct measurement of MAPD capacitance with deeply put pixels one should use the small alternative signal with frequency not more 100kHz .

-
- [1] Z.Y. Sadygov. Mikrokanalniy lavinniy fotodiod. Patent Rossii №2316848, prioritet ot 01.06.2006. (in Russian)
 - [2] Z.Y. Sadygov *et al.*, Performance of new mikro-pixel avalanche photodiode from Zecotek Photonics //2009, Nucl. Instr. Meth. A, 610, pp. 381-383.
 - [3] Z.Y. Sadygov *i dr.* Pisma v JTF, 2013, t. 39, vip. 11, s.7-12. (in Russian)
 - [4] Z.Y. Sadygov *et.al.* Three advanced designs of micro-pixel avalanche photodiodes: Their present status, maximum possibilities and limitations// 2006, Nucl.Instr. Meth. A,567, pp. 70-73.
 - [5] Z. Sadygov *et al.* Physics of Particles and Nuclei Letters, 2013, Vol. 10, n. 7, pp. 780–782.
 - [6] Z.Y. Sadygov *et.al.*, Fizika XIX, 2013, № 2, Sect. En, pp. 17-19.
 - [7] E.A. Jafarova *i dr.*, AMEA Xəbərləri, Fizika-texnika elmləri seriyası, fizika və astronomiya. 2013, №XXXII, № 2, s.526-33. (in Russian)

Received: 02.04.2014

KINETICS OF PHASE TRANSFORMATIONS IN CuIn₅Se₈ THIN FILMS

A.Ch. MAMEDOVA, N.K. KERIMOVA, D.I. ISMAYILOV

Institute of Physics of Azerbaijan National Academy of Sciences

AZ-1143, H.Javid ave., 33, Baku, Azerbaijan

amamedova@inbox.ru

The processes of phase formation and phase transitions in CuIn₅Se₈ thin layers allowing the carrying out of the continuous object shooting at thermal treatment different conditions are investigated by kinematic electronography method. It is shown, that amorphous films form at evaporation of synthesized compound and thermal spraying of binary compounds Cu₂Se and In₂Se₃ in ratio 1:5. The crystallization kinetic parameters of amorphous films of CuIn₅Se₈ are established. The crystal growth regularity, activation energy values of germ-formation and their further growth are obtained.

Keywords: crystallization kinetics, amorphous film, nano-thickness

PACS: 548. 74; 539,234

1. INTRODUCTIUON

The main method for determination of crystal structure and phase composition of thin layers is the electron beam diffraction on nanodimensional films. The essence of kinematic electronography method based on rapid electron diffraction on objects, the dimensions of which are commensurable ones with wavelength of incident radiation, is the fact that diffraction picture is fixed on moving photographic plate which is mechanically drawn. The stationary values of activation energies showing on phase transition end when whole material of different compositions taking part in process transits from the amorphous state into crystal one or from the one crystal modification into another one, are obtained by kinematic electronography for thin films of each compound. The coherently scattered electrons having the big sensitivity to relatively scattered substance allow us to fix the reaction beginning and follow its further motion. This method can't be considered as alternative one to X-ray spectrometry and other optic methods not applying to nano-thickness films. The kinematic electronography is the unique independent method for quantitative investigations of phase transformation kinetics taking place in nano-thickness amorphous and crystalline films: texture, polycrystalline, monocrystalline films. The data obtained by this method can't be found with enough definiteness by other above mentioned methods which aren't potentially suitable for films by thickness by several decades nanometers. The result interpretation obtained by kinematic electronography presents the big interest for semiconductor material science. They can be used for measurement of diffusion rates in thin layers based on optical measurements up to present time and give the direct comparison possibility of obtained result for thin films with data for massive samples.

2. EXPERIMENT TECHNIQUE

The very narrow strip is cut from total diffraction picture to obtain electron diffraction patterns by kinematic method with the help of shutters being in electron diffractograph EMR – 102. Using these shutters one can make the gap of any width. As diffraction maximum width on photo-plate increases with gap increase then the diffraction ring curvature strongly reveals with gap increase. However, the diffraction lines from

polycrystalline sample keep its width and sharpness within limits of gap width change. The gap width at photo-plate drawing is selected by shutter establishment and in dependence on primary beam intensity one can be established in limits 0,1; 0,3; 0,5mm. It should switch off the forepump and close the fore vacuum valve for neutralization of vibrations from vacuum forepump at electron diffraction pattern kinematic shooting.

The study complexity of kinetics amorphous film crystallization processes and appearance of new crystalline modifications in case of phase transformations is in the fact that the mechanism of crystallization center formation and their further growth is often unknown. The data on crystal growth mechanism and dependence of phase transformation rate on temperature one can obtain by studying of time-temperature dependences of amorphous film crystallization and thin crystal layers recrystallization with establishment of phase transition kinetic parameters.

The thin-film materials suitable for investigations by diffraction method of high-energy electrons are obtained by both evaporation of synthesized compound CuIn₅Se₈ and thermal spraying of binary compounds of Cu₂Se and In₂Se₃ compositions in ratio 1:5. At simultaneous and layer-by-layer precipitation of Cu₂Se and In₂Se₃ the evaporation sources which are tungsten baskets of conic profile lag behind each other on distance 150mm at height 50mm relatively to freshly cleaved NaCl and grids covered by celluloid serving as substrates. The vapor condensation is carried out on substrates being at room temperature in vacuum, the residual gas pressure in which is ~ 10⁻⁴ Pa. The precipitation rate is ~ 0,2 nm/sec. For prevention of re-evaporation and thin-film sample oxidation in case of their thermal treatment at high temperatures, the thin films are covered by celluloid thin layer so that they are involved in singular capsule. It should be noted that at temperatures 423K and higher the celluloid protective film destroys. For removal of such processes, the probabilities of oxidation in air and decomposition in the process of following thermal treatments at increased temperatures or at their long storage, the investigated samples are encapsulated by thin layers of amorphous carbon [1-2]. Taking into consideration the carbon layer thickness the total thickness of investigated objects doesn't exceed ~50nm.

The structural characteristics of CuIn₅Se₈ thin layers obtained on NaCl and KCl surfaces being at different temperatures and film phase composition formed by simultaneous and consistent evaporation of Cu₂Se and In₂Se₃ are studied on electron diffractograph EMR – 102.

3. RESULTS AND THEIR DISCUSSION

The layer-by-layer precipitation of Cu₂Se, In₂Se₃ on substrates being at room temperature leads to phase distribution on condensation plane corresponding to calculated component composition at both simultaneous evaporation and independent on evaporation order.

On the base of scheme of phase condensation distribution on the plane constructed according to experimental data obtained as the result of analysis of electron diffraction pattern taken from points situated from each other on distance 4mm, it is established that forming films are amorphous ones in substrate region where by calculation the triple compound of CuIn₅Se₈ composition should form. The diffuse lines of electron diffraction pattern from amorphous films contain values $S = 4\pi \sin \theta / \lambda = 30,52; 40,43; 60,85 \text{ nm}^{-1}$. The amorphous films forming in sufficiently wide region of condensation plane at temperature 383K crystallize with structural characteristics $a=0,572; c=1,162 \text{ nm}$ according with data for hexagonal compound $\alpha - \text{CuIn}_5\text{Se}_8$ given in [3].

With the aim to study of CuIn₅Se₈ amorphous film crystallization kinetics the isothermal kinematic electron diffraction patterns showing the crystallization process at 363, 373 and 383K are obtained. At temperatures higher 393-398K the abrupt phase transition takes place as the result of which the whole process of phase transformation kinetics can't be fixed from beginning till the end.

The kinematic electron diffraction pattern, on which the crystallization process of amorphous CuIn₅Se₈ at temperature 373K is registered, is given in fig.1.

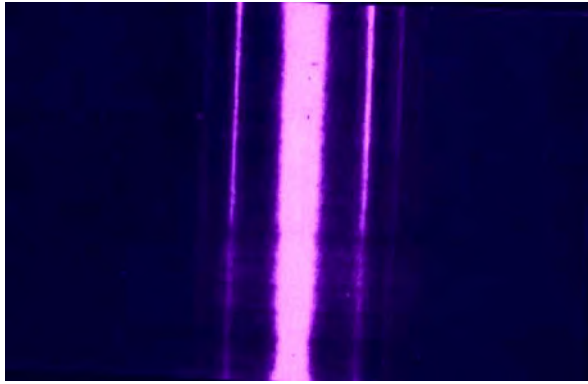


Fig 1. Kinematic electron diffraction pattern showing the phase transformation kinetics in CuIn₅Se₈ thin films.

The polycrystalline hexagonal CuIn₅Se₈ forms in the crystallization process. The diffuse lines of amorphous CuIn₅Se₈ totally disappear as the result of film annealing weakening with time and diffraction line intensities of crystal phase of hexagonal syngony increase.

The lines with (2021), (3142), (4042) indexes not overlapping with amorphous phase lines and neighboring crystal phase lines that could make mistakes

in intensity measurements, are chosen for both photometric definition and intensity electrometric measurement of CuIn₅Se₈ hexagonal diffraction lines in dependence on annealing time.

The intensity maximal value is compared with one of fully crystallized volume of investigated object for transition of intensity values to quantity of crystallized CuIn₅Se₈. The volume fitting on intensity unit is defined by the way that finally allows us to find the values of substance crystallized part volume in dependence on annealing time.

We use the following expression:

$$I_{hkl} = I_o \lambda \left| \frac{\Phi_{hkl}}{\Omega} \right|^2 V \frac{d_{hkl}^2 \Delta P}{4\pi L \lambda} \quad (1)$$

where I_o is primary beam intensity, λ is electron beam wave length, Φ is structural factor, Ω is elementary cell volume, V is radiated volume of polycrystalline substance, d_{hkl} is interplanar spacing, Δ is Debye ring small sector, P is multiplicity factor, $L\lambda$ is device constant.

The values of crystallized CuIn₅Se₈ in time moment V_t established for diffraction lines with above mentioned indexes are approximately identical ones; the difference doesn't exceed 3%. The dependences $\ln \ln \frac{V_o}{V_o - V_t}$ on $\ln t$ for temperatures 363K, 373K and 383K, expressed by direct lines, are presented in fig.2.

The comparison of isotherm data with following analytical expression

$$V_t = V_o [1 - \exp(-kt^m)] \quad (2)$$

established by Avrami-Kolmogorov for phase transformation kinetics shows that the best coincidence takes place at $m=4$. The value $m=4$ shows that in case of crystallization of amorphous CuIn₅Se₈ the three-dimensional crystal growth takes place. $\ln K$ values for 363, 373, 383K are equal to 25,7, 22,2 and 19,8 correspondingly. $\ln K$ dependence on reversal temperature for CuIn₅Se₈ is linear one.

According to Arrhenius equation:

$$\ln K = A - \frac{1}{RT} (E_{gf} + 3E_g), \quad (3)$$

where E_{gf} and E_g are activation energies of germ-formation and growth correspondingly. The sum value $E_{gf} + 3E_g$, defined by straight line inclination of $\ln K$ dependence on $1/T$, is equal to 87,7kcal/mol. The activation energy of germ-formation (E_{gf}), established from dependence $1/\tau_0$ on $1/T$, is equal to 21,4kcal/mol. The value of growth activation energy, obtained by equality $E_{tot.} = E_{gf} + 3E_g$, is equal to 22,1kcal/mol. Thus, it is established that at crystallization of amorphous CuIn₅Se₈ the values of activation energy necessary for crystallization center formation, i.e. germ-formation and their further growth have approximately identical values: 21,4 and 22,1 kcal/mol, that is very seldom.

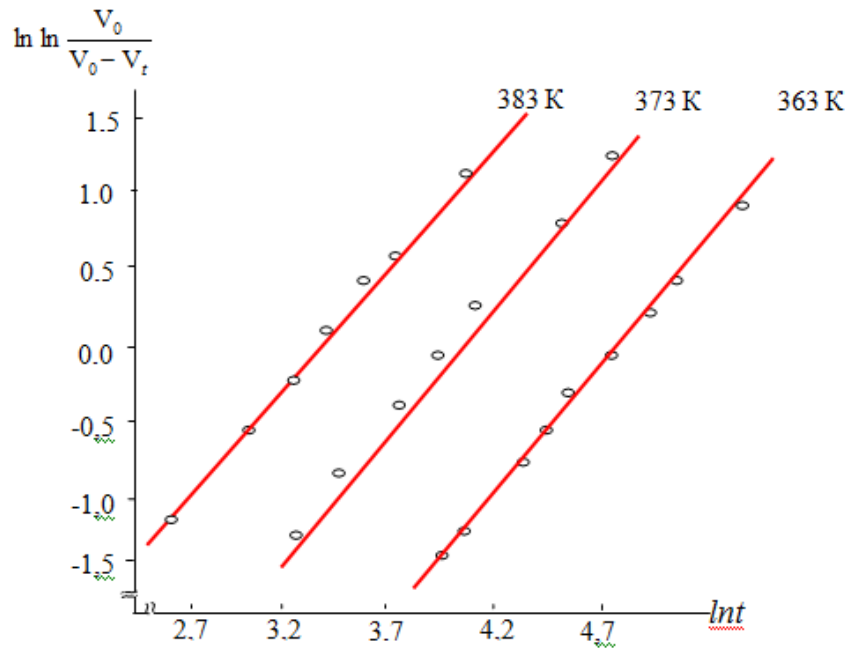


Fig.2. $\ln \ln \frac{V_0}{V_0 - V_t}$ dependence on lnt for crystallization of amorphous CuIn_5Se_8 .

CONCLUSION

The phase transformation kinetics in CuIn_5Se_8 amorphous films takes place on regularities established by Avrami-Kolmogorov and is described by analytical expression $V_t = V_0 [1 - \exp(-kt^m)]$. At crystallization of

CuIn_5Se_8 amorphous films, the three-dimensional crystal growth takes place. The activation energies of germ-formation and growth have approximately identical values: 21,4 and 22,1 kcal/mol.

-
- [1] A.Ch. Mamedova. Neorganicheskie materiali, t.44, №8, s. 911(2008). (In Russian).
 - [2] D.I. Ismailov, Doct.diss. Baku, Institut Fiziki NAN Azerbaydjana, 345s. (2007). (In Russian).
 - [3] L. Duran, S.M. Wasim, C.A. Durante Rincon, et al. Phys.stat.sol. V.199, № 2, 220 (2003).

Received: 02.04.2014

THERMAL EXPANSION, ISOTHERMAL COMPRESSION AND HEAT CAPACITY DIFFERENCE AT CONSTANT PRESSURE (C_p) AND CONSTANT VOLUME (C_v) IN SOLID SOLUTIONS $(\text{TlGaSe}_2)_{1-x}(\text{TlInS}_2)_x$ ($x = 0.1; 0.2$)

M.M. KURBANOV, M.M. GODJAYEV, A.M. AKHMEDOVA
Sumgayit State University

The temperature dependences of thermal expansion and isothermal compression of $(\text{TlGaSe}_2)_{0.9}(\text{TlInS}_2)_{0.1}$ and $(\text{TlGaSe}_2)_{0.8}(\text{TlInS}_2)_{0.2}$ are investigated. The heat capacity difference at constant pressure and volume ($C_p - C_v$) is calculated on the base of experimental data. It is established that $(C_p - C_v)$, which is connected with the increase of defect number and weakening of chemical bond in lattice, increases with temperature increase and increase of TlInS_2 content in composition.

Keywords: solid solution, structure, thermal expansion, isothermal compression, heat capacity, phase transition.

PACS: 72.15.Cz 65.40.De, 65.60.+a

The strongly anisotropic layered and chain semiconductors have the series of interest physical properties. Such compounds are also used for creation of laser facility and different of sensitive gauges. The calorimetric investigations and ones of photoconduction show that phase transition takes place in these crystals [1-3].

The thermal expansion, isothermal compression and heat capacity difference at constant pressure and constant volume ($c_p - c_v$) in solid solutions $(\text{TlGaSe}_2)_{0.9}(\text{TlInS}_2)_{0.1}$ and $(\text{TlGaSe}_2)_{0.8}(\text{TlInS}_2)_{0.2}$ are investigated in the present work with the aim to obtain additional information on phase transition and influence of crystal structure imperfection on thermodynamic parameters.

The solid solutions $(\text{TlGaSe}_2)_{0.9}(\text{TlInS}_2)_{0.1}$ and $(\text{TlGaSe}_2)_{0.8}(\text{TlInS}_2)_{0.2}$ are synthesized by two temperature method by the way of alloying of high purity initial elements [4]. The elementary cell parameters are

defined by X-ray method. It is established that solid solutions $(\text{TlGaSe}_2)_{1-x}(\text{TlInS}_2)_x$ ($x=0.1; 0.2$) crystallize in monoclinic syngony. The lattice parameters are: $a=10,512(2)\text{\AA}$, $b=10,578(2)\text{\AA}$, $c=15,030(2)\text{\AA}$, $\beta=100,6(3)^\circ$ for $(\text{TlGaSe}_2)_{0.9}(\text{TlInS}_2)_{0.1}$ and $a=10,531(2)\text{\AA}$, $b=10,598(2)\text{\AA}$, $c=15,630(2)\text{\AA}$, $\beta=100,6(3)^\circ$ for $(\text{TlGaSe}_2)_{0.8}(\text{TlInS}_2)_{0.2}$.

The thermal expansion and isothermal compression are measured by technique from [5] at 80-350K. The samples for measurements are prepared from synthesized ingots of cylindrical form of length 30mm and diameter 5mm. The error at measurements is 0,5%.

The measurement results of thermal expansion (α) and isothermal compression (χ_T) $(\text{TlGaSe}_2)_{0.9}(\text{TlInS}_2)_{0.1}$ and $(\text{TlGaSe}_2)_{0.8}(\text{TlInS}_2)_{0.2}$ are given on fig.1 and 2.

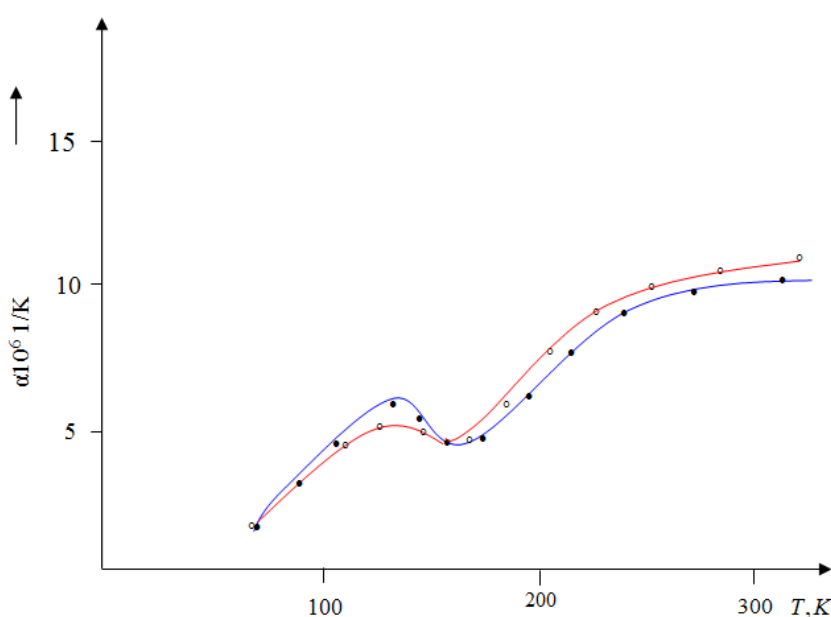


Fig. 1. Temperature dependence of thermal expansion coefficient of crystal system $(\text{TlGaSe}_2)_{1-x}(\text{TlInS}_2)_x$ where x : • -0,1; o - 0,2.

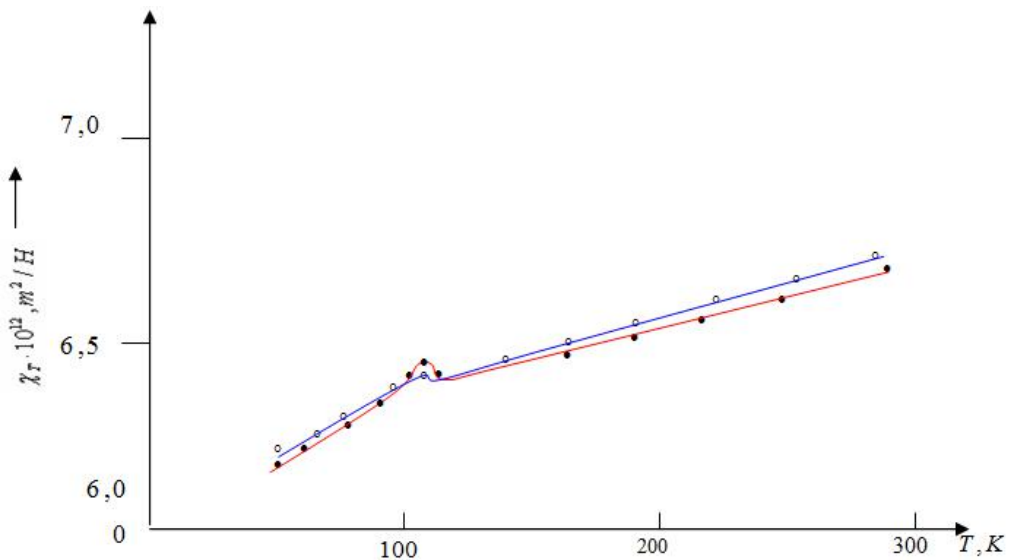


Fig. 2. Temperature dependence of thermal expansion coefficient of $(\text{TlGaSe}_2)_{1-x}(\text{TlInS}_2)_x$ crystals where x : \bullet - 0,1; \circ - 0,2

As it is seen the anomaly is observed in 105-120K interval on temperature dependences (α) and (χ_T). Such behavior of temperature dependence (α) and (χ_T) is probably connected with the fact that phase transition of second order takes place in the given temperature region. From fig.1 and 2 it is seen that the anomaly decreases with TlInS_2 of content increase in composition of solid solutions. Such behavior of (α) and (χ_T) can be connected with structure imperfection increase and weakening of interatomic chemical bond. The difference of heat capacity and constant pressure (C_p) and volume (C_v) is calculated on experimental data. The thermodynamic ratio is used for calculations [6].

$$C_p - C_v = \frac{\beta^2 VT}{\chi_T} \quad (1)$$

where β is volume coefficient of thermal expansion. The calculation results are given in table.

From the table it is seen that $(C_p - C_v)$ increases with temperature increase of heat capacity difference at constant pressure and constant volume. Besides, such increase takes place with TlInS_2 content increase in the composition. Such $(C_p - C_v)$ change proves that crystal imperfection degree increases and interatomic bond weakens with TlInS_2 content increase in the composition of solid solution.

Table

T, K	$(\text{TlGaSe}_2)_{0,9}(\text{TlInS}_2)_{0,1}$			$(\text{TlGaSe}_2)_{0,8}(\text{TlInS}_2)_{0,2}$		
	$\beta \cdot 10^6$ K^{-1}	$\chi_T \cdot 10^{12}$ m^2/N	$(C_p - C_v)$ J/kqK	$\beta \cdot 10^6$ K^{-1}	$\chi_T \cdot 10^{12}$ m^2/N	$(C_p - C_v)$ J/kqK
90	14.8	6.37	3.35	14.85	6.32	2.17
100	22.95	6.46	3.68	22.86	6.45	2.37
120	24.87	6.48	4.40	24.72	6.46	2.84
140	22.35	6.59	5.04	22.29	6.54	3.27
160	23.43	6.68	5.69	23.37	6.63	3.68
180	24.75	6.70	6.40	24.63	6.65	4.13
200	30.36	6.72	7.07	30.21	6.70	4.56
250	33.06	6.73	8.82	32.85	6.68	5.71
300	33.84	6.78	10.51	33.72	6.71	6.83

[1] M.M. Gojayev, G.D. Guseynov, E.M. Kerimova. Neorganicheskie materiali. 1987, t.23, n.12, s. 2087-2089. (in Russian)

[2] P.G. Rustamov, S.G. Abdullayeva, O.M. Aliyev i dr. Izv. AN SSSR. Neorganicheskie materiali. 1983, t.19, n. 3, s. 479. (in Russian)

THERMAL EXPANSION, ISOTHERMAL COMPRESSION AND HEAT CAPACITY DIFFERENCE AT CONSTANT...

- [3] V.A. Aliyev, M.A. Aljanov, S.N. Aliyev. Pisma v JETF. 1987, t. 45, vip. .9, s. 418- 420. (in Russian)
- [4] S.G.Abdullayeva, S.S. Abdinbekov, G.G. Guseynov. Dokl. AN Az. SSR. 1980, t. 26, n. 8. s. 34-38. (in Russian)
- [5] M.M. Kurbanov. Neorganicheskie materiali. 2001, t. 37, n. 12, s. 1447-1448. (in Russian)
- [6] N.P. Bazarov. Termodinamika, M: Vissn.shk., 1976, s. 78. (in Russian)

Received: 09.04.2014

ENERGY SPECTRUM AND SCATTERING MECHANISM OF CHARGE CARRIERS IN MONOCRYSTALLINE ALLOYS $\text{Bi}_{1-x}\text{Sb}_x$ ($0, \leq x \leq 0,25$) IN THE TEMPERATURE RANGE $T = 77\text{-}300\text{K}$

B.A. TAIROV, H.A. GASANOVA

Institute of Physics of Azerbaijan NAS, H.Javid ave.,33, Baku, AZ-1143

btairov@physics.ab.az, rasulova.khayala@mail.ru

The resistivity components ρ_{ij} , Hall coefficient R_{ijk} and magnetoresistance $\rho_{ij,kl}$ in monocrystalline alloys $\text{Bi}_{1-x}\text{Sb}_x$ at temperatures of 77-300K are measured. The possibility of quantitative interpretation of galvanomagnetic effects in bismuth and $\text{Bi}_{1-x}\text{Sb}_x$ alloys with $x \leq 0,09$ based on the model of electron Fermi surface in the form of three ellipsoids and holes, in the form of ellipsoid of rotation . In alloys and antimony of electron Fermi surface remains the same as in the bismuth; for holes in antimony it is in the form of six ellipsoids of general type and an ellipsoid of rotation. Hole Fermi surface in $\text{Bi}_{1-x}\text{Sb}_x$ with $0,16 \leq x \leq 0,25$ is represented as three ellipsoids general type being presumably in Σ ST point. The angle of inclination of the electron ellipsoids decreases with antimony content increase. Based on the analysis of anisotropy of hole mobilities, one can suggest, that hole ellipsoids in $\text{Bi}_{1-x}\text{Sb}_x$ alloys with $0,16 \leq x \leq 0,25$ are less anisotropic ones than the hole ellipsoids $\text{Bi}_{1-x}\text{Sb}_x$ with $0 \leq x \leq 0,16$, so anisotropy hole mobility in $\text{Bi}_{1-x}\text{Sb}_x$ alloys with $0,16 \leq x \leq 0,25$ $v_2/v_1 = 0,05$ and $v_3/v_1 = 0,5$ and in $\text{Bi}_{1-x}\text{Sb}_x$ alloys with $0 \leq x \leq 0,16$ $v_2/v_1 = 0,009$ and $v_3/v_1 = 0,7$. The current extremes and parameters of electrons in $\text{Bi}_{1-x}\text{Sb}_x$ alloys are established. It is shown that in $\text{Bi}_{1-x}\text{Sb}_x$ semi-metallic alloys at 77 - 200K, there is a mixed electron scattering equally with acoustic phonons, L - T interband electron scattering is effective one and fusion scattering of charge carriers predominates in $\text{Bi}_{1-x}\text{Sb}_x$ semiconductor alloys in 77 - 170K interval and at $T > 170\text{K}$ electrons efficiently disperse on acoustic phonons.

Keywords: scattering mechanism, solid solution, charge carriers

PACS: 64.75.Nx; 72.20.Pa

INTRODUCTION

Recently the interest in bismuth and $\text{Bi}_{1-x}\text{Sb}_x$ alloys has grown [1-2]. The small value of thermal conductivity and the small effective mass of electrons in $\text{Bi}_{1-x}\text{Sb}_x$ solid solutions allows us to use them in infrared sensors and thermoelectric generators, the characteristics of which are directly connected with energy spectrum and charge carrier scattering mechanism.

Therefore, in this paper, the study of galvanomagnetic effects in n - $\text{Bi}_{1-x}\text{Sb}_x$ to identify the energy spectra in these crystals, is carried out.

EXPERIMENTAL RESULTS AND DISCUSSION

The components of electric conduction, magnetoresistance and Hall coefficient are measured at constant current in magnetic fields 0-0,2Tl. The measurements are carried out in solenoid, the homogeneous field region of which is 0,15-0,2 along solenoid axis, its inner diameter is 0,1m.

It should be noted, that the values of the coefficients ρ_{ijk} and $\rho_{ij,kl}$ given in the paper, correspond to the conditions of a weak magnetic field. To obtain these values, the dependence of corresponding galvanomagnetic coefficient on the field is always taken. Moreover, the condition for weak magnetic field, i.e. the independence of R_{ijk} Hall coefficient and $\rho_{ij,kl}$ magnetoresistance, is controlled.

For quantitative interpretations of the experimental results on the galvanomagnetic properties of $\text{Bi}_{1-x}\text{Sb}_x$ the relations [3,4,5] between the components of the galvanomagnetic coefficients with electron and hole kinetic parameters

It should be noted that the given relations [3,4,5] remain in force in NENP model, as it is revealed in [6] that the presence of three symmetrically placed ellipsoids in $\text{Bi}_{1-x}\text{Sb}_x$ almost softens the anisotropy of kinetic

coefficients associated with the deviation of the dispersion law from ellipsoid form. Therefore, at calculation of kinetic phenomena, one can restrict by ENP and EP models. Such interpretation from one hand allows us to judge about correctness of the choice of energy spectrum model by the agreement of the experimental and calculated values, since at the assumption of relaxation time isotropy of carries the mobility tensor components characterize the components of the effective mass tensor.

To calculate the parameters of the energy spectrum of charge carriers in bismuth-antimony alloys on the base of experimentally obtained values of the galvanomagnetic coefficients, it is necessary to concentrate on the most obvious its model, which further will be confirmed by the comparison of experimental and calculated values. Firstly, let's go back to the schemes which demonstrate the energy spectrum variation of $\text{Bi}_{1-x}\text{Sb}_x$ alloys on the its composition (Fig. 1).

As it is seen from the figure at the content of antimony 6 at.%, the gap between the valence and the conduction bands opens, while the gap width is determined by L_a conduction band and T valence band. According to the model of Fermi surface (like pure bismuth) should include three ellipsoids of general type for electrons, inclined in respect of the basal plane, and the ellipsoid of rotation with axis in trigonal direction for holes.

When the content of antimony (8-12 at.%), the gap is determined between L_a and L_s energy distances, and the hole Fermi surface should be presented by three ellipsoids similar to electron one. However, T and Σ hole bands being near the bottom of the conduction band have the significantly higher density of states than L_s , whereby in alloys with antimony content up to 12 atm.%, they can play a major role in the transfer phenomena at temperatures higher than 77K.

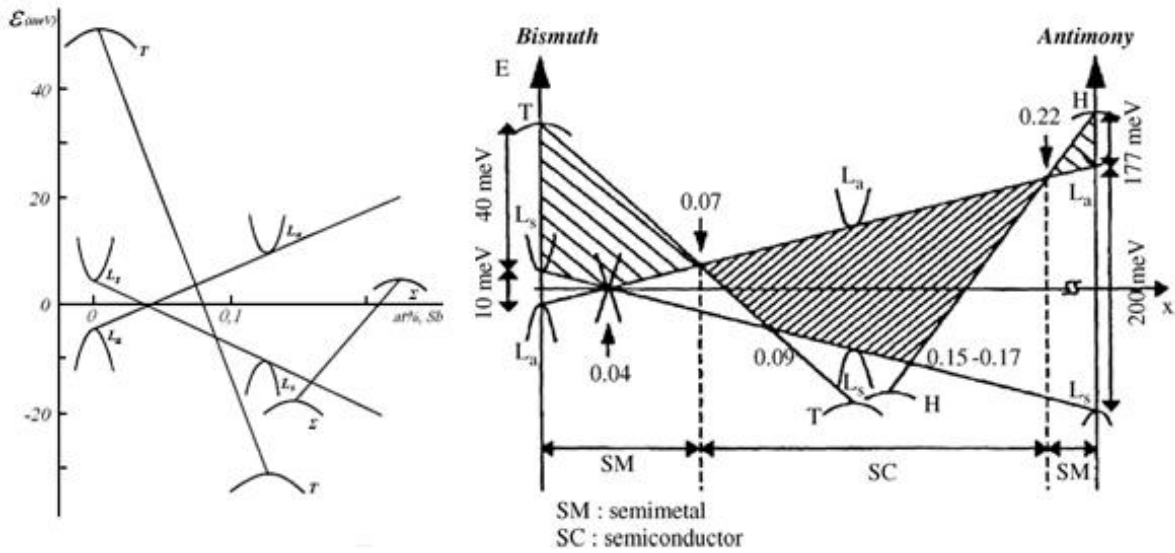


Fig.1. The schemes of energy spectrum reconstruction of bismuth-antimony alloys at increase of antimony concentration [7,8].

The new hole band the extremum of which presumably is H or Σ points begins to play role at further antimony content increase [9, 10]. The question, whether the new appeared hole band is one with extremum in H point as in pure antimony, which falls with antimony concentration increase on energy scale or this band is one with extremum in точке Σ point which rises from valence band depth of pure bismuth, is still open.

Note that the energy indirect gap between bands with extremum L_a point and appeared band decreases and is equal to zero at 22at% Sb with antimony content increase. $\text{Bi}_{1-x}\text{Sb}_x$ alloys become the semimetals at further antimony content increase.

According to above mentioned we use the model representing electron Fermi surface in the form of three ellipsoids general type easily inclined in respect to trigonal axis and placing in Brillouin zone in L point for interpretation of galvanomagnetic properties of $\text{Bi}_{1-x}\text{Sb}_x$ ($0,15 \leq x \leq 0,25$) alloys. Hole Fermi surface is represented by three or six ellipsoids general type inclined in respect to trigonal axis and placing in Σ and H points of BZ.

For antimony the electrons are in L point and holes are in H and GT points of Brillouin zone.

For interpretation of some $\text{Bi}_{1-x}\text{Sb}_x$ alloy properties especially at doping it is suggested that the carriers of additional bands take part in transfer phenomena are also used in works [11-12].

Thus, in general case the energy spectrum model of charge carrier in $\text{Bi}_{1-x}\text{Sb}_x$ alloys should take under consideration the possibility of charge carrier placement in L_a , L_s , T , Σ , H and GT bands.

Such model in general case can be described by three mobility components of L_a electrons (μ_1, μ_2, μ_3), three mobility components of L_s , Σ , H holes and Σ electrons (v_1, v_2, v_3), incident angle of electron and hole ellipsoids φ_e, φ_g correspondingly, concentration N_a, N_g and finally, by two mobility components of holes T and GT ($v_1 = v_2, v_3$) and concentration.

The ratios between above mentioned energy spectrum parameters and galvanomagnetic coefficients can be obtained in the assumption of contribution

independence into general charge carriers of different types.

The ratios obtained by such way are given in references [3,4,5].

The formula of the electric conduction expansion in the magnetic field is convenient by the fact that the obvious additivity of carrier contributions of separate bands is reflected. However, in experiment the resistance components in magnetic field, which are connected by ratio symmetry with corresponding components of electric conduction for D_{3d} crystals [13].

The ratios given in [13] towards the following condition:

$$N_a = N_g + N_g' \quad (1)$$

represent themselves the 13 levels with 13 in determinates (left parts of equations are experimentally obtained coefficients).

The ratios given in [13] towards with following condition:

$$N_e = N_g + N_g' \quad (1)$$

represent themselves the 13 levels with 13 unknown values (left parts of equations are experimentally obtained coefficients).

Thus, the solution of this nonlinear system of equations should lead to concrete definition of energy spectrum parameters. However, in analytical form it is impossible to solve this system of equation and that's why for this aim, the special programs with following solution selection which corresponds to physical meaning of obtained values are used.

The investigations of galvanomagnetic properties of $\text{Bi}_{1-x}\text{Sb}_x$ alloys are carried out in complex with of dispersion definition of Electromagnetic Magnetoplasma Waves (EMPW) the results of which are described in [14,15,16]. The important factor is the fact that EMPW propagation in Bi-Sb crystals is practically defined by

parameters of energy spectrum of L electrons and waves in hole plasma damp because of less hole mobilities (in undoped alloys). The definition of L electron parameters is also carried out with computer use and results of these experiments are used for the solving of above mentioned system of equations. Such use of investigation results of EMPW dispersion allows us to compare the correspondence of defined parameters by these two methods. As it is show in [17], the valence band in L point should be almost "mirror" for m_1 and m_3 directions in respect of conduction band, for m_2 direction the effective mass of halls is bigger in two times than one of electrons. That's why component ratios of L hole mobilities in m_1 and m_3 directions are equal to ones of L electron mobilities. Thus, the mobility structure of electrons and holes in L is defined.

The values of experimental and calculated values of galvanomagnetic coefficients for Bi, Sb and $\text{Bi}_{1-x}\text{Sb}_x$ alloys with antimony content 0÷25 at.% at temperature 77K are given in table 1. As it is seen from the table, for all alloy compositions the experimental and calculated values are in well agreement. It is necessary to note that agreement was only in narrow interval of values of concentration and charge carrier mobility, which are given in table 2. The values of experimentally defined and calculated values of galvanomagnetic coefficients in $\text{Bi}_{1-x}\text{Sb}_x$ alloys at $T=77$ K (σ_{11} , σ_{33} are measured with delicacy 3%, σ_{123} , σ_{231} – 5%, $\sigma_{11,22}$ – 10%, $\sigma_{11,11}$ and $\sigma_{33,11}$ – 15%, $\sigma_{11,33}$ and $\sigma_{33,33}$ – 20%; the dimension σ_{ij} is $\Omega^{-1} \text{cm}^{-1}$, σ_{ijk} is $\text{cm} \text{C}^1 \Omega^{-2}$, σ_{ijkl} is $\text{cm}^3 \text{C}^2 \Omega^{-3}$) are given in table 1.

Table 1

at.% Sb	type	$\sigma_{11} \times 10^{-5}$	$\sigma_{33} \times 10^{-5}$	$\sigma_{231} \times 10^{-7}$	$\sigma_{123} \times 10^{-6}$
0	Exp.	32,32	26,57	9,99	3,75
	Calc.	32,39	26,54	9,52	3,57
6	Exp.	12,44	15,94	8,7	2,77
	Calc.	11,8	14,64	8,72	2,98
9	Exp.	6,67	7,94	5,45	2,22
	Calc.	6,65	7,82	6,16	2,15
12	Exp.	4,8	5,3	2,72	0,84
	Calc.	4,6	5,4	3,07	0,83
16	Exp.	5,15	5,7	2	0,68
	Calc.	4,87	6,1	2,06	0,6
18	Exp.	6,25	7,8	2,2	0,58
	Calc.	6,03	7,7	2,26	0,59
20	Exp.	7,4	9,1	1,82	0,53
	Calc.	7,1	8,9	1,9	0,53
22	Exp.	7,94	9,6	1,28	0,34
	Calc.	7,53	9,38	1,38	0,31
25	Exp.	8,1	10,2	0,69	0,21
	Calc.	7,27	9,1	0,86	0,19
100	Exp.	141	198	0,63	7,2
	Calc.	145	192	0,58	7,14

Continuation of Table 1

at.%Sb	type	$\sigma_{11,33} \times 10^{-6}$	$\sigma_{33,11} \times 10^{-8}$	$\sigma_{11,11} \times 10^{-8}$	$\sigma_{11,22} \times 10^{-8}$	$\sigma_{33,33} \times 10^{-6}$
0	Exp.	220	34,66	19,92	59,4	106,24
	Calc.	200	35	17,8	54	108
6	Exp.	245	76,2	29,4	82,7	192
	Calc.	244	72,8	26	79,4	143
9	Exp.	284	70,4	35,7	95,2	171
	Calc.	278	79,1	28,6	86,1	155
12	Exp.	96	30,9	17,26	49,5	62
	Calc.	100	32	17,06	47,9	71
16	Exp.	34	10,7	5,84	14,2	19
	Calc.	39	14,3	5,1	15,6	20
18	Exp.	17,5	10,3	3,55	11,1	10,5
	Calc.	23,81	11,9	4,21	12,8	12
20	Exp.	11	7,5	2,62	7,85	8
	Calc.	17,23	7,2	2,6	7,85	7
22	Exp.	8,6	2,9	1,74	4,3	5,72
	Calc.	10,6	3,5	1,26	3,83	7,23
25	Exp.	5,3	1,16	1,01	1,97	2,23
	Calc.	4,35	1,47	0,53	1,6	2,98
100	Exp.	12,5	0,38	0,1	0,32	3,5
	Calc.	11,3	0,45	0,08	0,34	2,5

Table 2

 Kinetic parameters of charge carriers for $\text{Bi}_{1-x}\text{Sb}_x$ alloys at $T=77 \text{ K}$

at.% Sb	0	6	9	12	16	18	20	22	25	100
φ_3	$7^0 10$	$6^0 40$	$6^0 30$	$5^0 50$	5^0	$4^0 40$	$4^0 10$	$4^0 6$	$4^0 6$	$6^0 23$
φ_g				7^0	16^0	16^0	16^0	16^0	16^0	24^0
$\mu_1, \text{m}^2/\text{V}\cdot\text{s}$	74	120	172	179	90	71,5	52	34,4	23,2	1,83
$\mu_2, \text{m}^2/\text{V}\cdot\text{s}$	0,74	1,08	1,84	0,63	0,81	0,643	0,468	0,309	0,209	0,037
$\mu_3, \text{m}^2/\text{V}\cdot\text{s}$	37	84	112	92	63	50	36,4	24,1	16,2	1,42
$v_1, \text{m}^2/\text{V}\cdot\text{s}$				57	30	18	13	9,1	5,8	2,313
$v_2, \text{m}^2/\text{V}\cdot\text{s}$				0,24	1,5	0,9	0,65	0,455	0,29	0,296
$v_3, \text{m}^2/\text{V}\cdot\text{s}$				29	15	9	6,5	4,55	2,9	1,45
$v'_1, \text{m}^2/\text{V}\cdot\text{s}$	12,3	9,9	15,2							
$v'_2, \text{m}^2/\text{V}\cdot\text{s}$	12,3	9,9	15,2							
$v'_3, \text{m}^2/\text{V}\cdot\text{s}$	0,984	0,792	1,2							
N_s, m^3	$4,5 \times 10^{23}$	$1,1 \times 10^{23}$	$4,05 \times 10^{22}$	$2,4 \times 10^{22}$	$4,95 \times 10^{22}$	$8,21 \times 10^{22}$	$1,33 \times 10^{23}$	$2,1 \times 10^{23}$	$3,04 \times 10^{23}$	39×10^{24}
N_g, m^3				$2,4 \times 10^{22}$	$4,95 \times 10^{22}$	$8,21 \times 10^{22}$	$1,33 \times 10^{23}$	$2,1 \times 10^{23}$	$3,04 \times 10^{23}$	39×10^{24}
N'_g, m^3	$4,5 \times 10^{23}$	$1,1 \times 10^{23}$	$4,05 \times 10^{22}$							$4,88 \times 10^{24}$

On obtained results, one can make the conclusions:

1. The possibility of quantitative interpretation of galvanomagnetic effects in bismuth and $\text{Bi}_{1-x}\text{Sb}_x$ alloys with $x \leq 0,09$ based on the model of electron Fermi surface in the form of three ellipsoids and holes in the form of an ellipsoid of revolution, is shown.

2. In alloys and antimony of electron Fermi surface remains the same as in the bismuth; for holes in antimony these surfaces are presented in the form of six types of ellipsoids and an ellipsoid of rotation.

3. Hole Fermi surface in $\text{Bi}_{1-x}\text{Sb}_x$ with $0,16 \leq x \leq 0,25$ is represented as three ellipsoids of general type, being presumably in Σ point ZB.

4. The angle of inclination of electron ellipsoids decreases with antimony content increase. We note that a similar conclusion was reached in [18], where the dependence of angle of inclination of electron Fermi surface on composition for $\text{Bi}_{1-x}\text{Sb}_x$ alloys ($0 \leq x \leq 0,22$) is defined by dispersion investigation method EMPW.

5. Based on the analysis of hole mobility anisotropy one can suggest, that hole ellipsoids in $\text{Bi}_{1-x}\text{Sb}_x$ alloys with $0,16 \leq x \leq 0,25$ less anisotropic than the hole ellipsoids $\text{Bi}_{1-x}\text{Sb}_x$ with $0, \leq x \leq 0,16$ since anisotropy hole mobility in alloys for with $\text{Bi}_{1-x}\text{Sb}_x$ $0,16 \leq x \leq 0,25$ $v_2 / v_1 = 0,05$ and $v_3 / v_1 = 0,5$ and in Bi_xSb_x alloys with $0, \leq x \leq 0,16$ $v_2 / v_1 = 0,009$ and $v_3 / v_1 = 0,7$.

The temperature dependence of tensor component of mobility of electrons and holes in $\text{Bi}_{0,80}\text{Sb}_{0,20}$ alloys, multiplicity of obtained solutions are inside the sections designated on fig.2. As it is seen from the figure, all solutions are in very narrow intervals, evidencing on unambiguity of carried out calculations. The constructed dependence of mobility of electrons and holes averaged on three directions on temperature also evidences on

unambiguity of carried out interpretation (fig.3), all obtained values of averaged mobilities are in limits of confidence interval shown by line sections on plot.

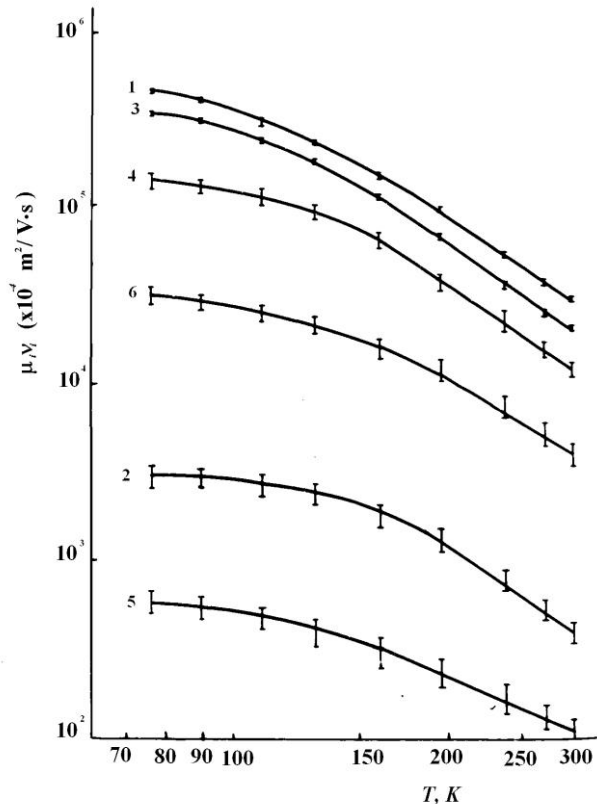


Fig. 2. Temperature dependence of the mobility tensor components of the electron and hole of alloy $\text{Bi}_{0,88}\text{Sb}_{0,12}$; 1 is μ_1 ; 2 is μ_2 ; 3 is μ_3 ; 4 is v_1 ; 5 is v_2 ; 6 is v_3 .

By other hand, for explanation of temperature dependence character of mobility and charge carrier concentration, one can use the simple two-band model [19] with averaging of directly measurement galvanomagnetic coefficients according to relations:

$$\frac{1}{\rho} = eN\mu \left(\frac{1}{b} + 1 \right) \quad (2)$$

$$R = \frac{1}{eN} * \frac{1-b}{1+b} \quad (3)$$

$$\frac{\rho \Delta \rho}{R^2 H^2} = \frac{b^2}{(b-1)^2} \quad (4)$$

and definition of averaged mobilities and charge carrier concentrations according to usual expressions for isotropic model.

$$\rho = \frac{1}{3}(2\rho_{11} + \rho_{33}) \quad (5)$$

$$R = \frac{1}{3}(2R_{231} + R_{123}) \quad (6)$$

$$\frac{\Delta \rho}{H^2} = \frac{1}{15}(\rho_{11,11} + 5\rho_{11,22} + 4\rho_{11,33} + 4\rho_{33,11} - 4\rho_{23,23} + 5\rho_{33,33}) \quad (7)$$

where b is ratio of mobilities of electrons and holes.

The values of averaged mobilities of electrons and holes, concentrations at different temperatures, calculated by such way, are also shown on figures 4,5 and 6.

on scattering mechanism of charge carriers can be carried out within the framework of representation $\mu \sim T^{-P}$.

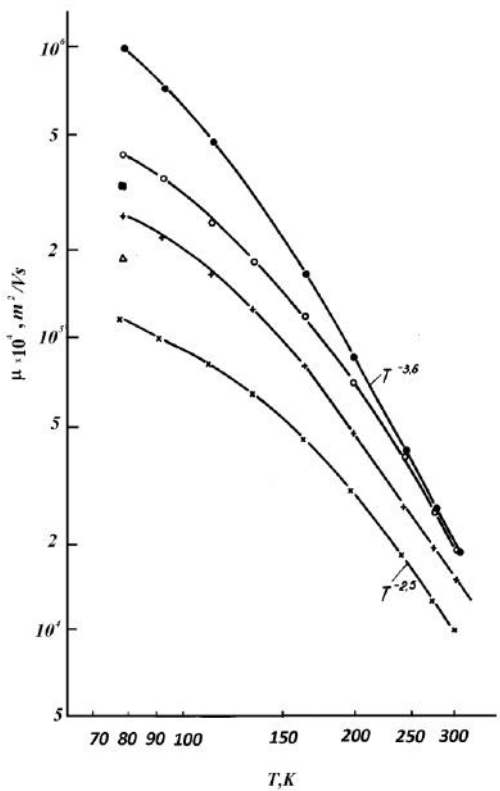


Fig. 4. Temperature dependence of the electron mobility:
 ● - Bi_{0.92}Sb_{0.08}; ○ - Bi_{0.84}Sb_{0.16}; ○+ - Bi_{0.88}Sb_{0.12};
 + - Bi_{0.80}Sb_{0.20}; Δ - Bi_{0.78}Sb_{0.22}; x - Bi_{0.75}Sb_{0.25};

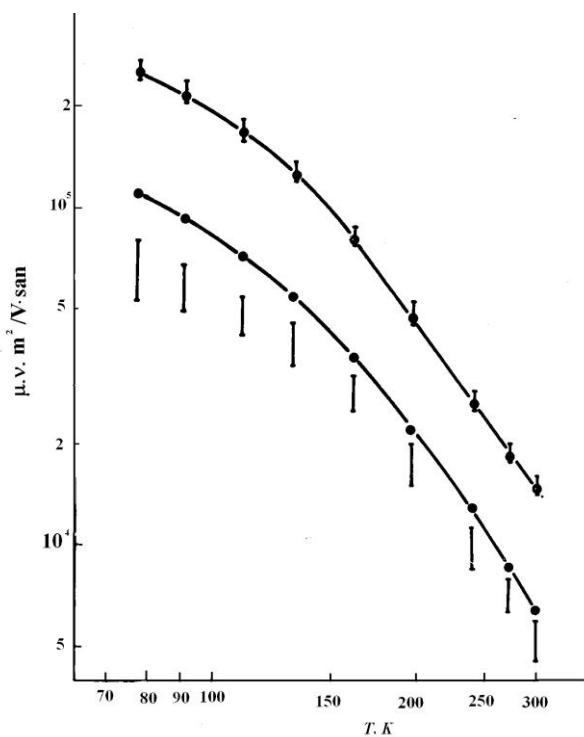


Fig.3. Temperature dependence of the carrier mobility in the alloy Bi_{0.80}Sb_{0.2}; ○ is electrons ● is holes v, calculated by the isotropic model, in the confidence intervals of electron and hole mobilities, averaged over the three directions.

Though these dependences can't be totally described with power functions on temperature, the possibility analysis of their explanation on the base of representation

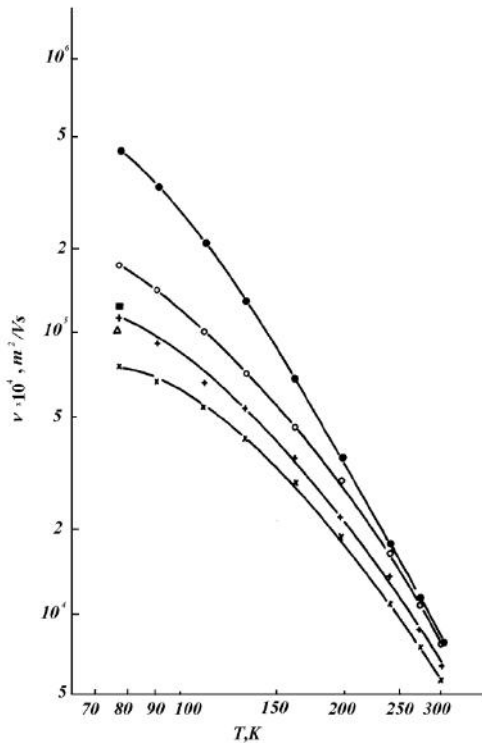


Fig. 5. The temperature dependence of the hole mobility:
 ● - Bi_{0.92}Sb_{0.08}; ○ - Bi_{0.84}Sb_{0.16}; ○+ - Bi_{0.88}Sb_{0.12};
 + - Bi_{0.80}Sb_{0.20}; Δ - Bi_{0.78}Sb_{0.22}; x - Bi_{0.75}Sb_{0.25};

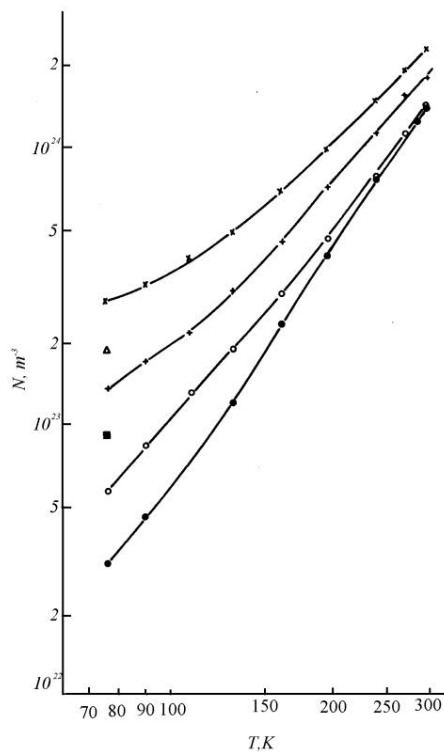


Fig. 6. Temperature dependence of the charge carrier concentration: ● - $\text{Bi}_{0.92}\text{Sb}_{0.08}$; ○ - $\text{Bi}_{0.84}\text{Sb}_{0.16}$; + - $\text{Bi}_{0.88}\text{Sb}_{0.12}$; - - $\text{Bi}_{0.80}\text{Sb}_{0.20}$; Δ - $\text{Bi}_{0.78}\text{Sb}_{0.22}$; ✕ - $\text{Bi}_{0.75}\text{Sb}_{0.25}$

First of all, it is necessary to note that temperature dependences of mobilities are defined by $P > 2.5$ degree. The dependence inclination of mobilities on temperature decreases with antimony content increase in solid solutions. If one can suppose that scattering on acoustic phonons and alloy disorders are the main ones, then temperature dependence of mobility should be defined by $P < \frac{3}{2}$ degree. The last one it is followed from the fact that scattering on disorders weakly depends on temperature and scattering on acoustic phonons gives $P < 3/2$. Thus, experimentally observable temperature dependences evidence on the presence of main scattering mechanism characterized by more strong temperature dependence. By other hand, in pure bismuth and $\text{Bi}_{1-x}\text{Sb}_x$ alloys with $0 \leq x \leq 0.10$ in temperature interval 77-200K, as it is shown in [20,25,26], the intervalley scattering caused by acoustic and optic phonons is the responsible for strong temperature dependence of electron mobility. In spite of the fact that acoustic phonons can play role in intervalley scattering in agreement of Korenblite work [21], the Lopez [22] calculations of matrix elements for acoustic and optic phonons show that intervalley scattering on optical phonons is effective one in 50 times than in acoustic ones.

If one can suppose that in Bi-Sb alloys like in pure bismuth, that strong temperature dependence of charge carrier mobility is responsible for intervalley scattering on acoustic phonons, then it is clear the change of temperature dependence inclination of charge carrier mobility on alloy composition. Indeed, according to [23] in Bi-Sb alloys the scattering on alloy disorders which

doesn't play the dominating role, but increases with increase of second component content, should be observed.

The relaxation time at scattering on alloy disorders is as follows: [24]

$$\tau = \frac{c}{x(1-x)} \quad (8)$$

where x is atom content of one of components, c depends on difference in atomic weights and difference of bond energy in lattices of components.

The mobility limited by scattering on alloy disorders is correspondingly proportional to $[m^*x(1-x)]^{-1}$. If we take under consideration the nonquadratic character of electron dispersion law, then their effective mass is proportional to $\sim N^{1/3}$.

The change of charge carrier concentration in Bi-Sb alloys with different antimony content in temperature interval 77-300K, is shown on fig. 6. As it is seen from the figure, the maximal change of charge carrier concentration is observed in alloys with antimony content 8 at%, so the relaxation time at scattering on alloy disorders weakly depends on temperature, the mobility change limited by this mechanism will be found by only effective mass change $\sim N^{1/3}$. Thus, according to fig.6, the mobility in interval 100-300K should change not more than in 3 times, whereas in experiment (see fig. 4) the mobility in the same temperature interval changes in 30 times, i.e. scattering on alloy disorders can't be the determinative one in mobility temperature dependence.

At the same time contribution of alloy disorder increases with antimony content increase according to expression (4), decreasing the inclination of experimentally observable temperature dependences of mobilities, moreover, intervalley distance becomes more dominant one and dependence inclination increases.

Analogously, the role of intervalley scattering on acoustic phonons leading to mobility change $\sim T^{-\frac{3}{2}}$ decreases with temperature increase.

The orienting differentiation of contributes of all three above mentioned scattering mechanisms can be carried out by the following way.

The presence of straight-line portion on experimental dependences $\lg\mu$ on $\lg T$ allows us to orientate in first approximation on such dependence, though at intervalley scattering the mobility temperature change can't be presented in the form of temperature exponential function.

Supposing that the intervalley scattering plays the dominating role at high temperatures we will obtain the value of electron mobility $\sim 2 \cdot 10^2 \text{ m}^2/\text{V} \cdot \text{s}$ for alloy with antimony content 8at% by extrapolation up to 77K.

By other hand, at this temperature, according to [23] the electron mobilities, limited by scattering on alloy disorders and acoustic phonons, are equal to $\sim 3 \cdot 10^2$ and $\sim 3,1 \cdot 10^2 \text{ m}^2/\text{V} \cdot \text{s}$.

Such detail coincidence one can consider occasional one, as above mentioned calculations have the orientation character because of supposition $\mu \sim T^P$, mobility averaging method and supposition of total domination of intervalley scattering at high temperatures. Nevertheless, the presence of such scattering mechanisms well

explains both the strong temperature dependence of mobility on temperature and dependence of its inclination on temperature and alloy composition.

If we calculate the total mobility from following relation $\frac{1}{\mu} = \sum \frac{1}{\mu_i}$ where μ_i are mobilities limited by three above mentioned mechanisms supposing the contribution independence of separate scattering mechanisms, then we will obtain the value $90 \text{ m}^2/\text{V}\cdot\text{s}$ coinciding with value obtained by experiment.

Note that in work [27] it is shown that electron mobility limited by scattering on alloy disorders is as follows:

$$\mu_{dis.} = \frac{2.1 \cdot 10^8 m^3}{x(1-x)V \cdot \text{sec}} \cdot n^{\frac{1}{3}} \quad (9)$$

and mobility limited by scattering on acoustic phonons has the following form:

$$\mu_{ac.} = \frac{1.1 \cdot 10^{25}}{m \cdot V \cdot \text{sec}} \cdot n^{-1} \quad (10)$$

The dependences of mobilities $\mu_{dis.}$ and $\mu_{ac.}$ on Bi-Sb alloy composition are shown in fig.7 (curve 1 and 2 correspondingly, total mobility is curve 3).

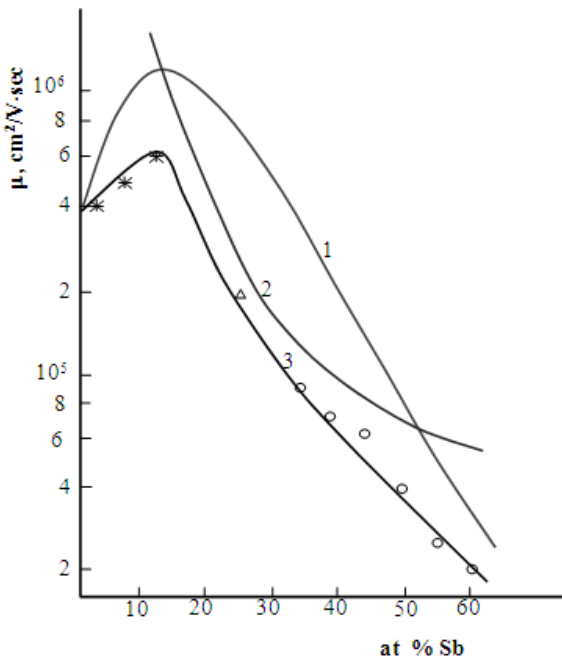


Fig. 7. The dependences of electron mobilities in $\text{Bi}_{1-x}\text{Sb}_x$ alloys on alloy composition at $T=77\text{ K}$: 1 is acoustic scattering; 2 is scattering on alloy disorders, 3 is total scattering.

Thus, in work it is shown that change of electron mobility in the dependence on Bi-Sb alloy composition (at $T=77^0 \text{ K}$) can be calculated taking into consideration the nonquadratic character of dispersion law and scattering charge carrier on acoustic branch of lattice oscillation spectrum and alloy disorders.

Electron effective mass in undoped bismuth is equal to $\sim 0.04m_0$ and on bottom of conduction band is equal to $\sim 0.0021m_0^*$. Then in [27] it is shown that:

$$\left(\frac{m^*}{m_0}\right)^2 = 1 + \frac{2h^2(3\pi^2n)^{\frac{2}{3}}}{m_0^* m_0 E_g} \quad (11)$$

Using (11) one can define the effective mass on the bottom of conduction band on known value of charge carrier concentration in undoped Bi-Sb. The calculation gives $0.0026m_0^*$ value that satisfactorily agrees with value $0.0021m_0^*$ calculated on experimental results [28]. Note that temperature dependence of averaged mobility found by calculation according to many-valley model practically coincides with dependence found according to isotropic one. Such agreement isn't occasional as it is mentioned above, if we suppose that ratio of mobility tensor components don't change with temperature increase then these dependences should coincide.

For hole mobilities the agreement between mobility values defined by these methods, also can be considered as satisfactory one, however, the difference between curves are essentially bigger than for electronic mobilities, besides, the value spread obtained at solving by computer is also essentially bigger one.

Such difference can be explained by following way: the electron mobility is essentially higher than hole one because of the fact that definition of last ones should be carried out with less accuracy. Besides, it is possible that in transition phenomena not only Σ holes but the ones of another band take part, the contribution of which is not essential one, but it can lead to some change of calculation results. At the same time the emphasis of this contribution we consider as inappropriate one as it is necessary to increase of the number of defined parameters and, therefore, the unambiguity of carried calculations.

Going to temperature change of charge carrier concentration, it is necessary to note that its definition on isotropic model gives more good results. Indeed, from figure 8 it is seen that many solutions obtained by computer gives the values totally coinciding with defined ones according to isotropic model.

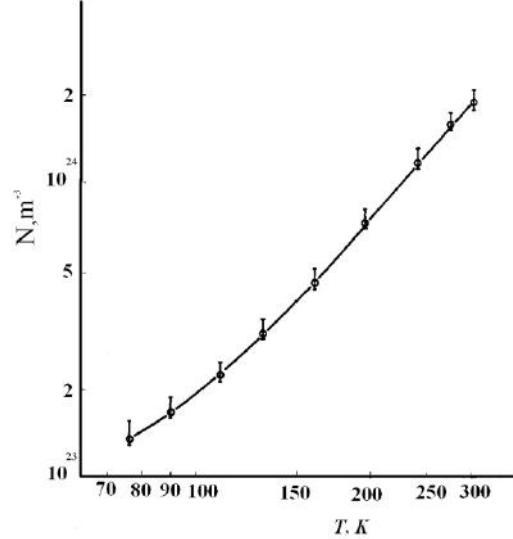


Fig.8. Temperature dependence of charge carrier concentration of $\text{Bi}_{0.80}\text{Sb}_{0.20}$ alloy; \circ is calculated on isotropic model; in confidence interval \bullet is calculated on multi-ellipsoid model.

Thus, character of concentration dependences of mobility components confirms the conclusion on change of actual extremum in valence band, made on the base of described above mentioned machine experiment.

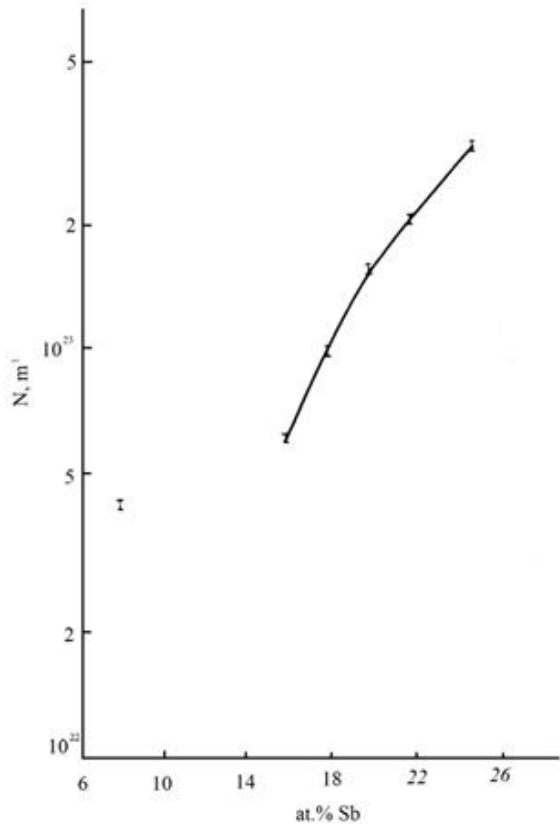


Fig.9. The dependence of charge carrier concentration on alloy composition at 77K.

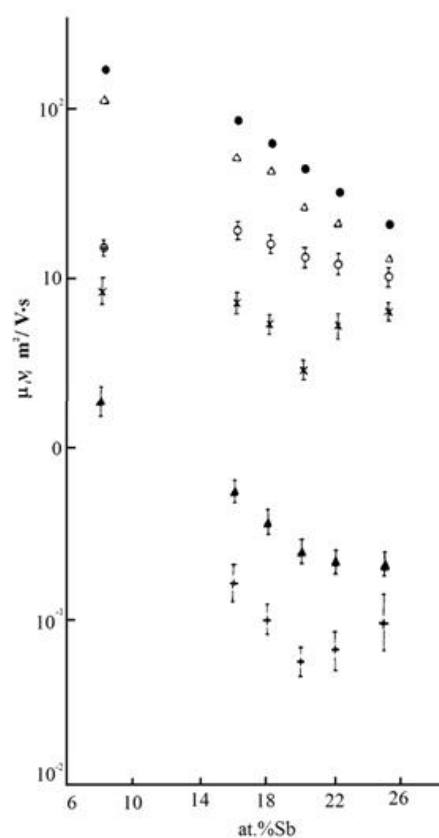


Fig.10. The dependence of mobility tensor components of electrons and holes of Bi-Sb alloys on antimony content at 77K.

The concentration changes of charge carriers and components on alloy composition at 77K are shown in figures 9,10. Let's consider the one of peculiarities of these dependences. As it is seen from the figures, the dependences on alloy composition of all mobility components and charge carrier concentration in antimony content interval 16÷25 at% present themselves the monotonously changing curves. At the same time, 8at%

corresponding to antimony content is obviously eliminated from these dependences. The last one can be evidence of change of band actual extremums.

Thus, character of concentration dependences of mobility components confirms the conclusion on change of actual extremum in valence band on the base of described above mentioned machine experiment.

- [1] *Lu Li, J.G. Checkelsky, Y.S. Hor, C. Uher, A.F. Hebard, R.J. Cava, N.P. Ong.* Science, **321** (5888), 547 (2008).
- [2] *D.Sh. Abdinov, T.D. Aliyeva, N.M. Axundova, M.M. Tagiyev.* Izv. NAN Azerbajijana. Ser. Fizika, **I** (5), **41** (2003). (in Russian)
- [3] *S.J. Freedman, H.J. Juretschke.* Phys. Rev., 1961, v. 124, N.5, p.1379-1386.
- [4] *B. Abeles, S. Meiboom.* Phys. Rev., 1956, v.101, n.2, p.544-550.
- [5] *R.N. Zitter.* Phys. Rev., 1962, v. 127, n.5, p. 1471-1480.
- [6] *I.M. Golban.* Issledovanie yavleniy perenosa v kristallakh tipa vismuta. Avtoreferat dis. na zvanie kand. fiz-mat. nauk. Kishinyov, 1982. (in Russian)
- [7] *N.B. Brandt, S.M. Chudinov, V.G. Karavaev.* JETF, 1976, t. 70, s. 2297-2317. (in Russian)
- [8] *Soma Dutta, V. Shubha, T.G.Ramesh* Effect of pressure and temperature on thermopower of Bi-Sb alloys. Elsevier Physica B. 405, 2010, p. 1239–1243.
- [9] *N.B. Brandt, S.M. Chudinov, V.G. Karavaev.* JETF, 1971, t.61, v. 2, s. 689-704. (in Russian)
- [10] *N.B. Brandt, Kh. Dittman, Y.G. Ponomarev.* FTT, 1971, t.13, v. 10, s. 2860-2872. (in Russian)
- [11] *V.S. Voloshin, V.M. Grabov, G.A. Ivanov, V.A. Kulikov, Y.N. Saraev, I.I. Fadeeva.* Tezisi dokladov po poluprovodnikam s maloy shirinoy zapreshonnoy zoni. Lvov, 1969. (in Russian)
- [12] *A.A. Averkin, Y.G. Vorov, G.A. Ivanov, B.L. Naletov, A.R. Regel.* FTT, 1971, t.13, n.12, s. 3644. (in Russian)
- [13] *H.J. Juretschke.* Acta Crystallogr., 1955, v.8, n.11, p.716-722.
- [14] *R. Brazis, J. Pozela, B. Tairov and M. Shakhtakhinskii.* Phys.Stat. Sol. (b), 1974, v.62, n2, p. 697-708.
- [15] *Y.K. Pojela, V. Rauka, B.A. Tairov, R. Tolutis.* Lit. fiz. sb., 1973, t. 13, v. 4, s. 535-543. (in Russian)
- [16] *V. Paulavichyus, Y.K. Pojela, R.Tolutis, B.A. Tairov.* Lit. fiz. sb., 1976, t. 15, v. 5, s. 771-779. (in Russian)

- [17] *M.I. Belovalov, N.B. Brandt, V.S. Vavilov, Y.G. Ponomarev.* JETF, 1977, t.73, n. 2(8), s. 721-731. (in Russian)
- [18] *W. Braune, B. Fellmuth, N. Kubicki, R. Herrman.* Phys. Stat. Sol. (b), 1982, v.110, n.2, p. 549 – 556.
- [19] *Y.T. Levitskiy, Y.G. Ivanov.* FMM, 1969, t.28, n. 5, s. 804-812. (in Russian)
- [20] *H. Nielsen.* J. Phys. F: Metal Phys., 1978, v.8, N.1, p.141 – 149.
- [21] *I.Y. Korenblit, M.E. Kuznetsov, V.M. Mujdaba, S.S. Shalit.* JETF, 1969, t. 57, v. 6(12), s. 1867-1876. (in Russian)
- [22] *A.A. Lopez.* Phys. Rev., 1968, v.175, N.3, p.823 – 840.
- [23] *M.I. Shakhtakhtinskaya, D.S. Tomtiev.* Izv. AN Azerb. SSR, ser. fiz. tekhn. i mat. nauk, 1973, n. 1, s. 46 – 51. (in Russian)
- [24] *D. Zayman.* Elektroni i fononi. M: IL, 1962, s. 488. (in Russian)
- [25] *B.A. Tairov, A. Sutkus, R. Tolitus, M.G. Shakhtakhtinskaya.* Temperaturnie zavisimosti effektivnoy koncentrachii I chiklotronnoy podvijnosti splavov $\text{Bi}_{0.91}\text{Sb}_{0.09}$ I $\text{Bi}_{0.85}\text{Sb}_{0.15}$. Dokladi AN Azerbaydjana, 1994. (in Russian)
- [26] *B.A. Tairov, A. Sutkus, R. Tolitus.* Temperaturnie zavisimosti podvijnosti i koncentrachii elektronov v polumetallicheskix splavax $\text{Bi}_{1-x}\text{Sb}_x$. Vestnik BQU, 1994, n.2., (in Russian)
- [27] *B.A. Tairov, V.A. Abdurakhmanova, H.A. Gasanova, M.A. Aslanov.* AJP Fizika, 2011, v. XVII, n. 4, p. 34-37.
- [28] *B. Lax, J.G. Mavroides , H.J. Zeiger and R. Keyes.* J. Phys. Rev Letters, 5, 241, 1960.

Received: 11.04.2014

EVOLUTION EQUATION OF WIGNER FUNCTION FOR RELATIVISTIC QUANTUM SYSTEMS

Sh.M. NAGIYEV, K.Sh. JAFAROVA

*Institute of Physics of Azerbaijan National Academy of Sciences
AZ-1143, H.Javid ave.,33,Baku, Azerbaijan*

The evolution equation for time-dependent Wigner distribution function and equation to define “distribution eigenfunctions” and energy eigenvalues of one-dimensional dynamic systems are obtained within the framework of relativistic finite-difference quantum mechanics.

Keywords: relativistic quantum system, finite-difference quantum equation, Wigner distribution function, evolution operator.
PACS: 02.70.Bf, 03.65.Fd, 03.65.Pm, 03.65.Ca.

INTRODUCTION

As it is known, there are several equivalent mathematic formulations of non-relativistic quantum mechanics. The quantum mechanical formulation in phase space uses only usual functions depending on p impulse, coordinate x and in general case on time t for description both states of physical systems and observable values. Phase representation gives the possibility to describe the quantum phenomena picture using the classic language as far as possible. In this representation Weyl symbols $A(p, x, t)$ are corresponded to operators $\hat{A}(\hat{p}, \hat{x}, t)$ and functions of system state are corresponded to distribution quantum functions $F^f(p, x, t)$ in it [1-6]. The fact, that phase representation uses only c-numerical values in of quantum mechanics but not operators, sometimes simplifies the mathematic description of quantum physical systems. The intensive application of phase representation in different fields of theoretical physics such as statistic physics, quantum optics, collision theory, nonlinear physics, is explained by this fact.

Wigner distribution functions [1], Glauber-Sudarshan functions [7,8], Khusimi functions [9],

Kirkvud functions [10], standard-ordered distribution function [11] are related to quantum distribution functions $F^f(p, x, t)$.

They are analogous ones to simultaneous probability density for p impulse and x coordinate but have the series of character peculiarities not allowing interpret them by such way. The noncommutativity of \hat{p} impulse operator and coordinates \hat{x} one is the reason preventing the introduction of simultaneous distribution of probabilities in quantum mechanics, i.e. the impossibility to measure quantum particle impulse and coordinate simultaneously. That's why in quantum mechanics one can find the probability distribution for coordinates and impulses separately but not simultaneously.

Consequently, the quantum distribution functions should be considered as mathematical tool simplifying the quantum calculations. They are called quasi-probability or quasi-density of probability simultaneous distribution p and x .

The general class of non-relativistic quantum distribution functions for pure states in coordinate representation in one-dimensional case is defined by the following formula [12]:

$$F_N^f(p, x, t) = \frac{1}{4\pi^2} \int_{-\infty}^{\infty} d\lambda d\mu dx' \psi_N^*(x' - \frac{1}{2}\mu\hbar, t) \psi_N\left(x' + \frac{1}{2}\mu\hbar, t\right) f(\lambda, \mu) e^{i\lambda(x'-x)} e^{-i\mu p}, \quad (1a)$$

and in impulse representation is defined by formula:

$$F_N^f(p, x, t) = \frac{1}{4\pi^2} \int_{-\infty}^{\infty} d\lambda d\mu dp' \phi_N^*\left(p' + \frac{1}{2}\lambda\hbar, t\right) \phi_N\left(p' - \frac{1}{2}\lambda\hbar, t\right) f(\lambda, \mu) e^{i\mu(p'-p)} e^{-i\lambda x}. \quad (1c)$$

Here $\psi_N(x, t)$ and $\phi_N(p, t)$ are non-relativistic wave functions of quantum system state in coordinate and impulse representations, correspondingly. The different quantum distribution function corresponds to different choice of $f(\lambda, \mu)$ function, for example, at $f(\lambda, \mu) = 1$ formula (1) gives the following expression for Wigner function:

$$\begin{aligned} W_N(p, x, t) &= \frac{1}{2\pi\hbar} \int_{-\infty}^{\infty} dx' \psi_N^*\left(x - \frac{x'}{2}, t\right) \psi_N\left(x + \frac{x'}{2}, t\right) e^{-i\frac{px'}{\hbar}} = \\ &= \frac{1}{2\pi\hbar} \int_{-\infty}^{\infty} dp' \phi_N^*\left(p + \frac{p'}{2}, t\right) \phi_N\left(p - \frac{p'}{2}, t\right) e^{-i\frac{p'x}{\hbar}} \end{aligned} \quad (2)$$

at $f(\lambda, \mu) = e^{-i\hbar\lambda\mu/2}$ formula (1) gives standard-ordered quantum function, at

$$f(\lambda, \mu) = \exp\left(-\frac{\lambda^2\hbar}{4m\kappa} - \frac{\mu^2 m\hbar\kappa}{4}\right)$$

it gives Khusumi function where κ is arbitrary positive constant. The exact expression for Wigner function for series of relativistic quantum-mechanical systems is discussed in scientific literature [2-5] and 13-16].

Wigner representation for relativistic models of linear oscillator describing the finite-difference equation [17, 18] is considered in [19, 20].

The aim of present work is to obtain the equation for Wigner relativistic function. Our task is formulated within framework of finite-difference version of relativistic quantum mechanics [21-25]. Here the conception of relativistic configuration r - space introduced in [22] plays the key role.

The corresponding canonically conjugated to r -space the impulse p -space is Lobachevsky three-dimensional space realized on upper margin of mass hyperboloid $p_0^2 - \hat{p}^2 = m^2 c^2, p_0 > 0$

The finite-difference variant of relativistic quantum mechanics has many character properties of non-relativistic quantum mechanics. The essential difference is in the fact that the wave function in relativistic representation satisfies to finite-difference equation. In one-dimensional case it has the following form:

$$i\hbar\partial_t \psi(x, t) = [H_o + V(x, t)]\psi(x, t), \quad (3)$$

where free Hamiltonian is as follows

$$H_o = mc^2 \cosh(i\tilde{\lambda}\partial_x), \partial_x = \partial/\partial_x \text{ and } V(x, t)$$

is non-stationary potential. The one-dimensional plane waves of following form

$$\xi(p, x) = \left(\frac{p_0 - p}{mc} \right)^{-ix/\tilde{\lambda}} \equiv e^{ix/\chi} \quad (4)$$

are eigenfunctions of free Hamiltonian, i.e. $H\xi = E_p \xi$,

$$\text{where } \chi = \ln\left(\frac{p_0 + p}{mc}\right) \text{ is rapidity,}$$

$$E_p = cp_0 = c\sqrt{p^2 + m^2 c^2}.$$

The connection between relativistic configuration x - and impulse p -representations is given with the help of relativistic Fourier transformation

$$\psi(x, t) = \frac{1}{\sqrt{2\pi\hbar}} \int \xi(p, x) \phi(p, t) d\Omega_p \quad (5)$$

where $d\Omega_p = mc \frac{dp}{p_o} = mcd\chi$ is invariant element of

integration in Lobachevsky p -space. The conditions of completeness and orthogonality for functions (4) have the form:

$$\begin{aligned} \frac{1}{2\pi\tilde{\lambda}} \int_{-\infty}^{\infty} \xi^*(p, x) \xi(p', x) dx &= \delta(\chi - \chi'), \\ \frac{1}{2\pi\tilde{\lambda}} \int_{-\infty}^{\infty} \xi^*(p, x) \xi(p, x') d\chi &= \delta(x - x'). \end{aligned} \quad (6)$$

EVOLUTION EQUATION FOR WIGNER RELATIVISTIC FUNCTION

According to present analogy between finite-difference relativistic quantum mechanics and non-relativistic one in works [19-20] Wigner relativistic function is defined similarly to non-relativistic case (2):

$$W(p, x, t) = \frac{1}{2\pi\hbar} \int_{-\infty}^{\infty} \psi^*\left(x + \frac{x'}{2}, t\right) \psi\left(x - \frac{x'}{2}, t\right) e^{ixx'/\tilde{\lambda}} dx', \quad (7a)$$

$$= \frac{1}{2\pi\tilde{\lambda}} \int_{-\infty}^{\infty} \phi^*\left(\chi + \frac{\chi'}{2}, t\right) \phi\left(\chi - \frac{\chi'}{2}, t\right) e^{-ixx'/\tilde{\lambda}} d\chi'. \quad (7b)$$

As dynamics of relativistic quantum system in considered case is defined by finite-difference equation (3) then Wigner function $W(p, x, t)$ also will satisfy to finite-difference evolution equation. To find this equation we use the work (3). But firstly in equation (3) we chose the potential energy in form $V(x, t) = V_0(x, t) e^{i\lambda\partial_x}$, where $\lambda = \alpha\tilde{\lambda}$, $\alpha \in R$. Using the expression for density matrix $\rho(x_1, x_2, t) = \psi(x_1, t)\psi^*(x_2, t)$ we have:

$$i\hbar \frac{\partial \rho}{\partial t} = \left[-2mc^2 sh\left(\frac{i\tilde{\lambda}}{2}\partial_x\right) sh\left(i\tilde{\lambda}\partial_x\right) + \left(V_0(x - \frac{x'}{2}, t) e^{i\frac{\lambda}{2}\partial_x} - V_0^*(x + \frac{x'}{2}, t) e^{-i\frac{\lambda}{2}\partial_x} \right) e^{-i\lambda\partial_{x'}} \right] \rho, \quad (8)$$

where we take $x_1 = x - x'/2, x_2 = x + x'/2$ in correspondence with formula (7a).

Differentiating (7a) and substituting (8) and further using the obvious following ratios

$$V_0\left(x - \frac{x'}{2}, t\right) e^{i\chi x'/\lambda} = V_0\left(\hat{X}^*, t\right) e^{i\chi x'/\lambda}, \quad (9a)$$

$$\int_{-\infty}^{\infty} f(x) e^{i\alpha \partial_x} \varphi(x) dx = \int_{-\infty}^{\infty} \varphi(x) e^{-i\alpha \partial_x} f(x) dx, \quad (9b)$$

we obtain the evolution equation for Wigner function:

$$i\hbar \frac{\partial W}{\partial t} = \left[-2mc^2 sh\chi sh\left(\frac{i\lambda}{2} \partial_x\right) + \left(V_0\left(\hat{X}^*, t\right) e^{\frac{i\lambda}{2} \partial_x} - V_0^*\left(\hat{X}, t\right) e^{-\frac{i\lambda}{2} \partial_x} \right) e^{-\alpha x} \right] W, \quad (10)$$

where $\hat{X} = x - \frac{i\lambda \partial_x}{2}$.

Formula (9b) is finite-difference analogue of integration by parts and is right for of $f(x)$ and $\varphi(x)$ functions, which are infinitely differentiable and vanishing at infinity towards with all derivatives

The method for determination of so-called “distribution eigenfunctions” and spectra of different physical values is supposed in work [26] (see also [27]). The integral equation for finding of quantum distribution eigenfunctions and functions of energy eigenvalues are given for example. We obtain the finite-difference analogue of this equation, i.e. the relativistic finite-difference equation for quantum Wigner distribution function of system stationary states.

Let's again use equation for $\rho(x_1, x_2) = \psi(x_1)\psi^*(x_2)$:

$$\left[mc^2 (\cosh(i\lambda \partial_{x_1}) + \cosh(i\lambda \partial_{x_2})) + V_0(x_1) e^{i\lambda \partial_{x_1}} + V_0^*(x_2) e^{-i\lambda \partial_{x_2}} \right] \rho(x_1, x_2) = 2E\rho(x_1, x_2). \quad (11)$$

Here wave functions $\psi(x_i)$, $i = 1, 2$ are solutions of stationary relativistic motion finite-difference equation:

$$\left[mc^2 \cosh(i\lambda \partial_{x_i}) + V_0(x_i) e^{i\lambda \partial_{x_i}} \right] \psi(x_i) = E\psi(x_i), \quad (12)$$

E is system energy.

Doing the same as at derivation of equation (10) we obtain the equation for relativistic Wigner function of stationary states:

$$\left[2mc^2 \cosh \chi \cosh\left(\frac{i\lambda}{2} \partial_x\right) + \left(V_0(\hat{X}^*) e^{\frac{i\lambda}{2} \partial_x} + V_0^*(\hat{X}) e^{-\frac{i\lambda}{2} \partial_x} \right) e^{-\alpha x} \right] W(p, x) = 2EW(p, x). \quad (13)$$

One can easily check that equations (10) and (13) in non-relativistic limit $c \rightarrow \infty$ transform into corresponding non-relativistic ones:

$$i\hbar \frac{\partial W_N}{\partial t} = \left[-\frac{i\hbar p}{m} + V\left(x + \frac{i\hbar}{2} \partial_p, t\right) - V\left(x - \frac{i\hbar}{2} \partial_p, t\right) \right] W_N(p, x, t), \quad (14)$$

$$\left[-\frac{\hbar^2}{2m} \partial_x^2 + \frac{p^2}{m} + V\left(x + \frac{i\hbar}{2} \partial_p\right) + V\left(x - \frac{i\hbar}{2} \partial_p\right) \right] W_N = 2E_N W_N(p, x). \quad (15)$$

It should be noted that as in non-relativistic case [27] the relativistic stationary Wigner distribution functions $\left(\frac{\partial W}{\partial t} = 0\right)$ being the solutions of equation (13) should satisfy simultaneously to equation (10). By other words, jointly solving the equations (10) and (13), one can find the eigenfunctions and eigenvalues of equation (13) and also thermodynamically equilibrium distribution function.

CONCLUSION

In the present paper we derivate the relativistic one-dimensional equations: evolution equation for non-stationary Wigner functions and eigenvalue equation for stationary ones. At $c \rightarrow \infty$ these equations transform

into corresponding non-relativistic equations for non-stationary and stationary Wigner function.

The given paper is supported by Science Development Foundation under the President of the Republic of Azerbaijan which is **Grant № EIF-2012-2(6)-39/08/1**

- [1] *E.P. Winger*, Phys Rev. 40 (1932) 749.
- [2] *M. Hillery, R.F.O. Connell, M.O. Scully, E.P. Winger*. Phys.Rep. 106 (1954) 121-167
- [3] *V.I. Tatarskiy*, UFN 139 (1983) 587. (in Russian).
- [4] *H.W.Lee*, Phys.Rep. 259 (1995) 147-211.
- [5] *N.L.Balazs, B.K. Jennings*. Phys.Rep. 104 (1984) 347-391.
- [6] *T.E. Moyal*. Proc.Cambridge Philos. Soc. 45 (1949) 99.
- [7] *R.J. Glauber*. Phys.Rev. 131 (1963) 2766.
- [8] *E.C.G.Sudarshan*. Phys.Rev. Lett. 10(1963)277.
- [9] *K. Husimi*. Proc. Phys.Math.Soc.Japan 22(1940) 264.
- [10] *T.G. Kirkwood*. Phys.Rev. 44(1933) 31.
- [11] *C.L. Mehta*. J.Math. Phys. 5(1964) 677.
- [12] *L. Cohen*. J.Math. Phys. 7(1966) 781 .
- [13] *R.W. Davies, K.T.R. Davies*. Ann.Phys. 89(1975) 261.
- [14] *V.V. Doodonov, V.I. Manko, O.V. Shakmistrova*. Phys.Lett. A 102(1984) 295.
- [15] *Frank, A.L. Rivera, K.B. Wolf*. Phys.Rev. A 61(2000) 054102-1
- [16] *S. Nouri*. Phys.Rev. A 57(1998) 1526.
- [17] *N.M. Atakishiev, R.M. Mir-Kasimov, Sh.M. Nagiev*. TMF 44 (1980) 47. (in Russian).
- [18] *R.M. Mir-Kasimov, Sh.M. Nagiyev, E.D. Kagramanov*. 1987, The relativistic linear oscillator in a homogeneous external field and the bilinear generating function for the Pollaczek polynomials, Preprint №214(Inst. of Physics, Azerbaijan Academy of Sciences) p.12
- [19] *N.M. Atakishiyev, Sh.M. Nagiyev, K.B. Wolf*. Theor. Math.Phys.144 (1998) 322.
- [20] *S.M. Nagiyev, G.H. Guliyeva, E.I. Jafarov*. J.Phys. A:Math.Theor.42 (2009) 454015.
- [21] *V.G. Kadyshevsky, R.M. Mir-Kasimov, N.B. Skachkov*. Nuovo Cim. 55(1968) 233.
- [22] *V.Q. Kadishevskiy, R.M. Mir-Kasimov, N.B. Skachov*. ECHAYA 2 (1972) 635. (in Russian).
- [23] *K.A. Milton, I.L. Solovtsov*. Mod.Phys.Lett. A16(2001) 2213.
- [24] *Sh.M. Nagiyev, E.I. Jafarov, R.M. Imanov, L. Homorodean*. Phys.Lett. A334(2005) 260.
- [25] *Sh.M. Nagiyev, S.I. Guliyeva*. Phys.Lett. A373 (2009) 2810.
- [26] *Yu.L. Klimontovich*. DAN SSSR 108 (1956) 1033. (in Russian).
- [27] *E.P. Boqdanov, V.I. Qorshenkov, V.L. Konkov*. Izv. vuzov SSSR, Fizika №7(1970) 94. (in Russian).

Received:16.04.2014

ELECTRONIC STRUCTURE AND CONFORMATIONAL-DYNAMIC PROPERTIES OF ALLATOSTATIN MOLECULE

L.I. VELIYEVA, E.Z. ALIYEV

Baku State University

AZ-1148, Baku, Z. Khalilov str., 23

Lala_Veliyeva@rambler.ru

The electronic structure and conformational-dynamic properties of allatostatin molecules are investigated in present work by MNDO and MM+ methods; the stable elements of spatial structure are revealed; the quantitative estimation of dihedral angle change limit of peptide molecule main chain in the process of dynamic reconstruction is carried out.

Keywords: neuro-peptides, structure, conformational-dynamic properties

PACS: 87.80.-y

INTRODUCTION

The study of electronic structure and conformational-dynamic properties of biological molecules including neuro-peptides, becomes the more actual one in the connection with development high level of computer technologies and the more distribution of corresponding program products. The investigations in this direction are also actual ones from solving of modern science main problem point of view, connected with establishment of interconnection between molecule structure and their functional activity. The neuro-peptides of allatostatin assemblage having the unique ability to regulate the processes of synthesis and secretion of juvenile hormones of insect different types can be related to the object of last decade intensive investigation [1-4]. The allatostatin assemblage includes the peptide molecules known as allatostatines I-IV or Dippu-ASTs.

The dynamic properties of allatostatin molecules are investigated in the given work by method of molecular mechanics MM+ ; the stable elements of spatial structure are revealed; the quantitative estimation of dihedral angle change limit of peptide molecule main chain in the process of dynamic reconstructions is carried out. The allatostatin electronic structure is also investigated by semiempirical method of quantum chemistry MNDO in standard parameterization and the comparative analysis of obtained results is carried out.

CALCULATION METHODS

The methods of quantum chemistry and molecular dynamics are wide spread in numerical modeling of electron and atomic structures of complex molecular systems. Nowadays the enough many calculative complexes realizing the calculations by methods of quantum chemistry and molecular dynamics are known. The complex of quantum-chemical and molecular-dynamic programs **HyperChem** is related to the number of such functioning program products. All results of electron and molecular-dynamic modeling presented in the given work are obtained with the use of this program the demonstration version of which is available on site <http://www.hyper.com> [5-7]. The calculated models of molecules are constructed on the base of atom coordinates obtained by method of theoretic conformational analysis within framework of atom mechanical model [8-11]. The

optimal neuro-peptide electronic structure is established in optimization process of valent electron energy at fixed coordinates of atom nuclei. At electronic structure calculation the molecule general charge in ground state is equal to zero. The values of total, atomic and electron energies of molecules and dipole moments are calculated; the charge distribution on atoms of molecules is investigated. The change character of atom partial charges in dependence on conformational states of molecules under consideration is studied. N-end of neuro-peptide is modified by acetyl (ACE) and C-end is modified by N-methylamine (NME) with formation of two additional peptide bonds with the aim of decrease of edge effect from strongly polar end groups.

CALCULATION RESULTS AND THEIR DISCUSSION

The low-energy allatostatin conformational states before and after molecular dynamics carried out during 30psec at constant temperature 273K are shown in fig.1-4. The neuro-peptide molecule relaxation with use of force field MM+ is carried out before calculation. The electron parameters of molecules under consideration are calculated by MNDO methods

Allatostatin I. *Allatostatin I* is neuro-peptide in chemical structure of which there are thirteen amino-acid residuals Ala1-Pro2-Ser3-Gly4-Ala5-Gln6-Arg7-Leu8-Tyr9-Gly10-Phe11-Gly12-Leu13. The conformation corresponding to conformational energy global minimum according to conformational analysis data and conformation obtained in the end of dynamic transformations in molecular dynamic process are shown on fig.1a. The analysis of obtained results shows that during first five picoseconds the molecule energy strong changes take place, further the fluctuation character becomes the monotonous in simulation process. The energy achieves its minimum value in the end of time interval (5-30psec) that evidences about spatial structure stabilization. As it is followed from calculation results the peptide chain sector Leu8-Leu13 forming β -turn is more stable in comparison with Ala1-Gln6 sector on N-end of peptide molecule. This result is agree with conformational analysis data according to which β -turn on Leu8-Leu13 sector realizes in 70% of calculated low-energy states of *allatostatin I* molecule.

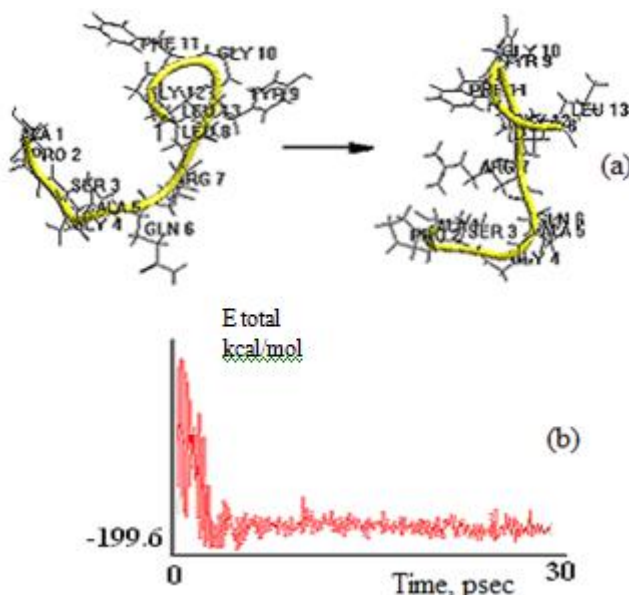


Fig. 1. Conformational transformations (a) and total energy change (b) of *allatostatin I* molecule in molecular dynamics process.

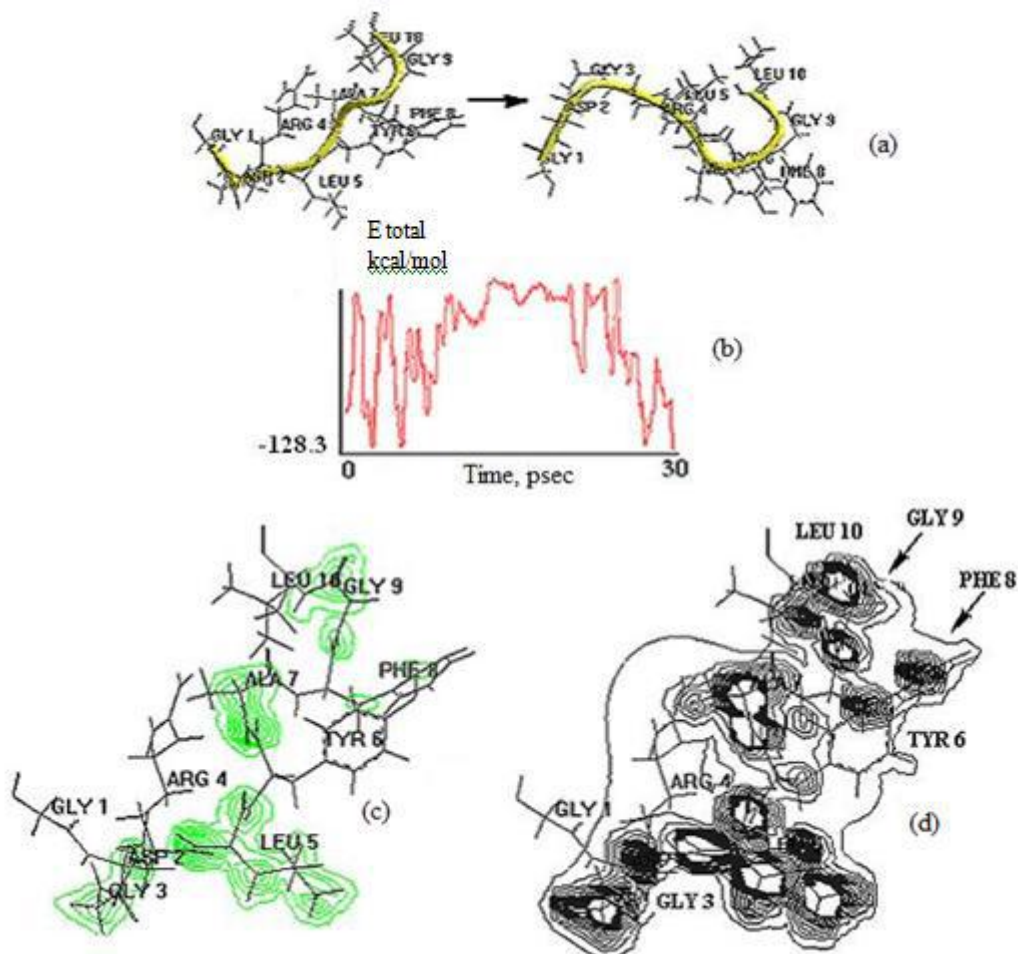


Fig.2. Conformational transformations (a), total energy change (b), distribution of electrostatic potential (c) and charge density (d) on XY plane obtained for *allatostatin II*.

Allatostatin II. Allatostatin II is neuro-peptide consisting of consistency of decade amino-acid residuals Gly1-Asp2-Gly3-Arg4-Leu5-Tyr6-Ala7-Phe8-Gly9-Leu10. The conformation corresponding to global minimum of conformational energy according to conformational analysis data is shown in fig.2a. [8]. The molecule contains the residual (Arg4) with positively charged side

radical and residuals with aromatic side chains (Tyr6, Phe8). The negatively charged carboxylated group of aspartic acid side chain (Asp2) and volume side chain in leucine residual (Leu10) are also related to the number of functionally important groups defining the peculiarities of molecule spatial structure. According to results of conformational analysis, the presence of labile C-end

sector at relatively hard N-end fragment is the peculiarity of molecule spatial structure. As it is followed from calculation results the molecule energy change has the non-monotonous character, the energy fluctuation during whole dynamic process is observed. The strong energy decrease which achieves the minimum value ~128.3kcal/mol is observed in simulation end. The formation of two β -turns, in top of which there are residuals Arg4 and Phe8, is observed in *allatostatin II* spatial structure. The quantum-chemical calculations by MNDO method are carried out after molecule relaxation. Any quantum-chemical calculation is based on system energy minimization of N electrons and M nuclei. The minimum search methods allow us to find the point on potential energy surface corresponding to molecule equilibrium configuration with less energy (or minima if they are several ones). The choice of initial geometry and symmetry of molecule plays the important role: taking account right symmetry the calculation time can reduce in several times because of decrease of variable parameter number.

The conjugated gradient method is used in calculations. The quantum-chemical method is also used for calculations of dipole moments and construction of electrostatic potential distribution picture and charge

density for allatostatin molecules. The molecular electrostatic potential is defined by electron density $\rho(r)$ and nucleus charges Z. The potential characterizes the electrostatic interaction energy between molecular (negative and positive) charge distribution and positive infinitely small unit charge.

Allatostatin III. *Allatostatin III* is neuro-peptide with primary structure containing the consistency from nine amino-acid residuals Gly1-Gly2-Ser3-Leu4-Tyr5-Ser6-Phe7-Gly8-Leu9.

The start structure for molecular-dynamic calculations corresponds to state with minimum value of conformational energy obtained as a result of conformational analysis of *allatostatin III* molecule [9]. As it is followed from calculation results the strong change of molecule energy in simulation process takes place during first five picoseconds.

The distance increase between end groups of Gly1 and Leu9 residuals (increase takes place in limit 6.1÷7.3 Å) which doesn't destroy the character elements of *allatostatin III* molecule spatial structure is the result of such change, in particular, the folded structure on Leu4-Phe7 section doesn't change during molecular dynamics.

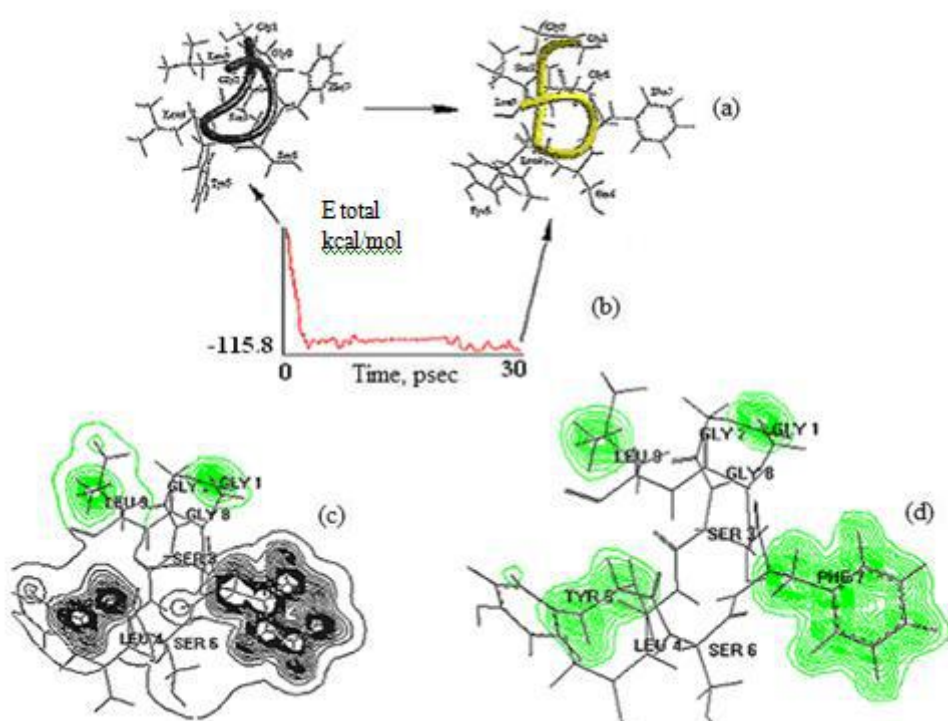


Fig.3. Molecular dynamic of *allatostatin III* (a), change of molecule total energy (b), distribution of electrostatic potential (c) and charge density (d) on XY plane

Allatostatin IV. There are eight consistently connected amino-acid residuals Asp1-Arg2-Leu3-Tyr4-Ser5-Phe6-Gly7-Leu8 in primary structure of *allatostatin IV*. The conformation corresponding to global minimum of conformational energy according to conformational analysis data shown in fig.4a [10,11].

The significant conformational mobility of N-end consistency in comparison with tetra-peptide fragment Tyr4-Leu8 is established in molecular dynamics process.

The energy change has the non-monotonous character, achieves the maximum value at 12psec, further the monotonous decrease and further relaxation of molecule structure takes place.

The obtained results will be used for molecular modeling of neuro-peptide analogues and study of their structural-functional interaction with the aim of revealing of spatial structure general elements responsible for pharmacological effects of investigated compounds.

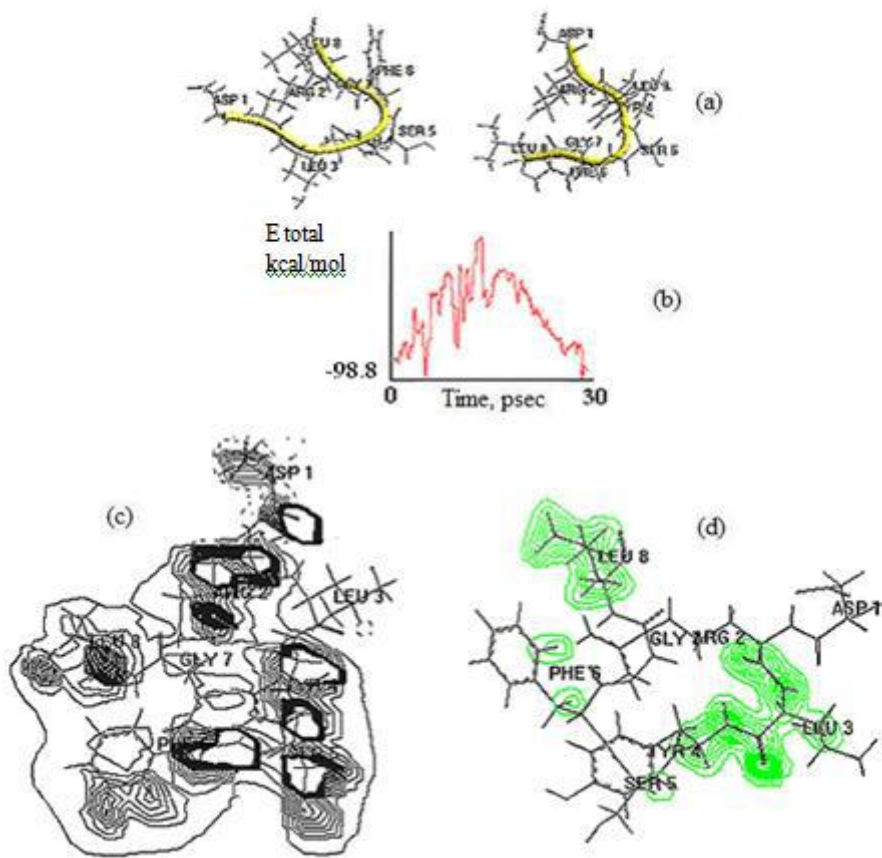


Fig.4. Molecular dynamics of *allatostatin IV* (a), molecule total energy change (b), distribution of electrostatic potential (c) and charge density (d) on XY plane.

1. *D. Veelaert, B. Devreese, L. Schoofs et al.* «Izolation and characterization of eight myoinhibiting peptides from the desert locust, *Schistocerca gregaria*: new members of the cockroach allatostatin family» // Mol.Cell Endocrinol., 1996, v.122 (2), p.183-190.
 2. *D. Veelaert, B. Devreese, L. Schoofs et al.* «Izolation and characterization of schistostatin-2 (11-18) from the desert locust, *Schistocerca gregaria*: a truncated analog of schistostatin-2» // Regulatory peptides, 1996, v.67 (3), p.195-199.
 3. *W.G. Bendena, B.C. Donly, S.S. Tobe.* «Allatostatins: A growing family of neuropeptides with structural and functional diversity» // Ann.N.-Y.Academy of Sciences, 1999, v.897, p.311-329.
 4. *J.P. Edwards, N. Audsley, G.C. Marris, R. Weaver.* «The role of allatostatic and allotropic neuropeptides in the regulation of juvenile hormone biosynthesis in *Lacanobia oleracea*» // Peptides, 2001, v.22(2), p.255-261
 5. *E.E. Shnol, A.G. Grivtsov i dr.* «Metod molekulyarnoy dinamiki v fizicheskoy khimii» M.: Nauka, 1996. (In Russian)
 6. K.V. Shaytan, S.S. Saraykin. «Metod molekulyarnoy dinamiki» 1999, <http://www.moldyn.ru/library/md/default.htm>. (In Russian)
 7. <http://www.hyper.com>
 8. *L.I. Veliyeva, M.A. Musayev, I.N. Aliyeva.* «Strukturnoe issledovanie molekuli allatostatina-II». V materialakh Mejdunarodnoy nauchnoy konferentsii «Molekulyarnie, membrannye i kletochnye osnovi funktsionirovaniya biosistem», Minsk, Belarus, 2006, s.111-113.
 9. *I.N. Aliyeva, L.I. Veliyeva, M.A. Musayev, N.M. Gojayev.* «Conformational features of the Dippu-AST 8 neuropeptide from Cockroach *Diptoptera punctata*» // Protein and Peptide Letters, 2006, v.13, p.1007-1015.
 10. *M.A. Musayev, L.I. Veliyeva, I.N. Aliyeva, N.M. Gojayev.* Vestnik Bakinskogo Universiteta, seriya fiz. mat. nauk, 2005, n.2, s.167-178. (In Russian)
 11. *L.I. Veliyeva, M.A. Musayev, I.N. Aliyeva, N.M. Gojayev.* Vestnik Bakinskogo Universiteta, seriya fiz. mat. nauk, 2006, n.1, s.120-13. (In Russian)

Received: 16.04.2014

HIGGS BOSON PRODUCTION IN ELECTRON-POSITRON ANNIHILATION

S.Q. ABDULLAYEV, M.Sh. GOJAYEV, F.A. SADDIGH

Baku State University, Az-1148, Z.Khalilov, 23, Baku, Azerbaijan

s.abdullayev@mail.ru, f_seddig@yahoo.com

In the framework of Standard Model the process of scalar Higgs boson production in electron-positron annihilation has been investigated: $e^-e^+ \Rightarrow H\bar{f}\bar{f}$. It is shown that, this process is defined by only four helicity amplitudes F_{LL}, F_{LR}, F_{RL} and F_{RR} , which describe following reactions: $e_L^-e_R^+ \Rightarrow Hf_L\bar{f}_R$, $e_L^-e_R^+ \Rightarrow Hf_R\bar{f}_L$, $e_R^-e_L^+ \Rightarrow Hf_L\bar{f}_R$ and $e_R^-e_L^+ \Rightarrow Hf_R\bar{f}_L$. The cross sections are calculated for spiral processes and analytic expressions are obtained for the left-right spin asymmetry A_{LR} and the degree of fermion longitudinal polarization p . It is verified that left-right spin asymmetry A_{LR} depends only on coupling constants of electron and it is of order of 14%, the degree of fermion polarization p depends only on coupling constant of fermion, and reaches to 67% (for $u\bar{u}$ - and $c\bar{c}$ -quark pair production) or 90% (for $d\bar{d}$ -, $s\bar{s}$ - and $b\bar{b}$ -pair production). At the energy $\sqrt{s} = 500 \text{ GeV}$ the energy distributions of Higgs boson are studied.

Keywords: Higgs boson, Helicity, left and right coupling constants, left-right spin asymmetr Weinberg's parameter, degree of longitudinal polarization.

PACS: 12.15.-y; 12.15.Mm; 14.70.Hp

INTRODUCTION

The Weinberg-Salam unified theory of Electromagnetic and Weak interaction (Standard Model-SM) has achieved great success [1, 2]. It includes the prediction of neutral weak current, discovery of W^\pm - and Z^0 -gauge bosons and some of its claims are investigated successfully in experiments. One of the important acclaims of SM is the prediction for the existence of scalar Higgs boson. Some experiments are carried out for the discovery of Higgs boson in different Experimental Labs.

Finally in Tevatron and CERN new information are received concerning the existence of Higgs boson with the mass of 125 GeV [3-6]. So the channels which give rise to Higgs bosons have got more attentions.

1. The amplitude and cross section of process:

In this work the annihilation of e^-e^+ -pair with longitudinal polarization is studied for the sake of production of Higgs boson and fermion-antifermion pair with longitudinal polarization:

$$e^-(p_1, \lambda_1) + e^+(p_2, \lambda_2) \Rightarrow H(k) + f(q_1, h_1) + \bar{f}(q_2, h_2). \quad (1)$$

Here $p_1(\lambda_1)$, $p_2(\lambda_2)$, $q_1(h_1)$ and $q_2(h_2)$ are 4-momentum (helicity) for electron, positron, fermion and antifermion and k is the 4-momentum of Higgs boson.

The Feynman diagram for the process (1) is shown in Fig. 1. According to this diagram, e^-e^+ -pairs first an-

nihilate to Z^0 -boson and Z^0 in turn transforms to fermion-antifermion pair while emitting Higgs boson.

We know that the Lagrangian for interaction of fermions with Z^0 -boson and Z^0 -bosons with Higgs boson can be written as follow [1]:

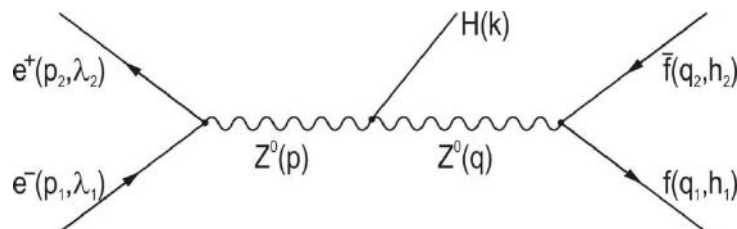


Fig. 1. Feynman diagram for the process $e^-e^+ \Rightarrow H\bar{f}\bar{f}$.

$$L_{ffZ} = \frac{e}{2} [g_L^{(f)} \bar{f} \gamma_\mu (1 + \gamma_5) f + g_R^{(f)} \bar{f} \gamma_\mu (1 - \gamma_5) f] Z_\mu, \quad (2)$$

$$L_{ZZH} = \frac{eM_z}{2 \sin \theta_W \cdot \cos \theta_W} \cdot Z_\mu Z_\rho g_{\mu\rho} H(k). \quad (3)$$

Here

$$g_L^{(f)} = \frac{I_f^{(3)} - Q_f \sin^2 \theta_W}{\sin \theta_W \cdot \cos \theta_W}, \quad g_R^{(f)} = -Q_f \tan \theta_W, \quad (4)$$

Are constants for interaction of left and right handed fermions with Z^0 -boson, θ_W – is the Weinberg angle, $I_f^{(3)}$ and Q_f are third projection of the weak isospin and electric charge of fermion respectively.

According to (2) and (3) we can write the transition amplitude for this process as

$$M = \frac{e^2}{4} \cdot \frac{e M_Z}{2 \sin \theta_W \cdot \cos \theta_W} \bar{v}(p_2, \lambda_2) \gamma_\mu [g_L^{(e)}(1 + \gamma_5) + g_R^{(e)}(1 - \gamma_5)] u(p_1, \lambda_1) \times \\ \times D_{\mu\rho}(p) D_{\rho\nu}(q) \bar{u}(q_1, h_1) \gamma_\nu [g_L^{(f)}(1 + \gamma_5) + g_R^{(f)}(1 - \gamma_5)] v(q_2, h_2). \quad (5)$$

Here

$$D_{\mu\rho}(p) = \left(-g_{\mu\rho} + \frac{p_\mu p_\rho}{M_Z^2} \right) \cdot \frac{1}{p^2 - M_Z^2 + i M_Z \Gamma_Z} \quad (6)$$

is the propagator of Z^0 -boson, $p = p_1 + p_2$, $q = q_1 + q_2 = p - k$, M_Z and Γ_Z are the mass and total width of Z^0 -boson.

At high energies we can neglect the mass of electron and fermions which will cause in conservation of weak currents:

$$p_\mu \bar{v}(p_2, \lambda_2) \gamma_\mu [g_L^{(e)}(1 + \gamma_5) + g_R^{(e)}(1 - \gamma_5)] u(p_1, \lambda_1) = 0, \\ q_\nu \bar{u}(q_1, h_1) \gamma_\nu [g_L^{(f)}(1 + \gamma_5) + g_R^{(f)}(1 - \gamma_5)] v(q_2, h_2) = 0.$$

Following this, the transition amplitude (5) takes a simpler form:

$$M = \frac{e^2}{4} \cdot \frac{e M_Z}{2 \sin \theta_W \cdot \cos \theta_W} \cdot D_Z(s) D_Z(xs) \cdot \bar{v}(p_2, \lambda_2) \gamma_\mu [g_L^{(e)}(1 + \gamma_5) + g_R^{(e)}(1 - \gamma_5)] \times \\ \times u(p_1, \lambda_1) \bar{u}(q_1, h_1) \gamma_\mu [g_L^{(f)}(1 + \gamma_5) + g_R^{(f)}(1 - \gamma_5)] v(q_2, h_2). \quad (7)$$

Here

$$D_Z(s) = (s - M_Z^2 + i M_Z \Gamma_Z)^{-1}, \quad x = 1 - \frac{2\omega}{\sqrt{s}} + \frac{M_H^2}{s},$$

and s is the total energy of electron and positron in the center of mass system, M_H and ω are the mass and energy of Higgs boson respectively.

Let's discuss some of the properties of transition amplitude M for the annihilation of electron and positron with longitudinal polarization. The interaction between electron and Z^0 -boson has a vector and axial-vector components. This circumstance leads to conservation of the helicity of the electrons at high energies. The conservation of helicity requires the electron and positron to have opposite helicities: $e_R^- e_L^+$ or $e_L^- e_R^+$. Here e_L^- is the electron with left polarization ($\lambda_1 = -1$) and e_R^+ represents the positron with right polarization ($\lambda_2 = 1$).

Final fermion-antifermion pairs should have same characteristics: $f_L \bar{f}_R$ or $f_R \bar{f}_L$. So for the reaction (1) only four independent helicity amplitudes will arise: F_{LL} , F_{LR} , F_{RL} and F_{RR} (here first and second indices show the helicity of electron and fermion). Those helicity amplitudes describe the following reactions:

$$e_L^- + e_R^+ \Rightarrow H + f_L + \bar{f}_R, \quad e_L^- + e_R^+ \Rightarrow H + f_R + \bar{f}_L, \\ e_R^- + e_L^+ \Rightarrow H + f_L + \bar{f}_R, \quad e_R^- + e_L^+ \Rightarrow H + f_R + \bar{f}_L.$$

In the framework of SM the amplitude, (7) can be written as

$$M = \frac{e^2}{4} \cdot \frac{e M_Z}{2 \sin \theta_W \cdot \cos \theta_W} \times$$

$$\begin{aligned} & \times \left\{ F_{LL} [\bar{v}(p_2, \lambda_2) \gamma_\mu (1 + \gamma_5) u(p_1, \lambda_1)] [\bar{u}(q_1, h_1) \gamma_\mu (1 + \gamma_5) v(q_2, h_2)] + \right. \\ & + F_{LR} [\bar{v}(p_2, \lambda_2) \gamma_\mu (1 + \gamma_5) u(p_1, \lambda_1)] [\bar{u}(q_1, h_1) \gamma_\mu (1 - \gamma_5) v(q_2, h_2)] + \\ & + F_{RL} [\bar{v}(p_2, \lambda_2) \gamma_\mu (1 - \gamma_5) u(p_1, \lambda_1)] [\bar{u}(q_1, h_1) \gamma_\mu (1 + \gamma_5) v(q_2, h_2)] + \\ & \left. + F_{RR} [\bar{v}(p_2, \lambda_2) \gamma_\mu (1 - \gamma_5) u(p_1, \lambda_1)] [\bar{u}(q_1, h_1) \gamma_\mu (1 - \gamma_5) v(q_2, h_2)] \right\}. \end{aligned} \quad (8)$$

Here

$$\begin{aligned} F_{LL} &= D_z(s) D_z(xs) g_L^{(e)} g_L^{(f)}, & F_{LR} &= D_z(s) D_z(xs) g_L^{(e)} g_L^{(f)}, \\ F_{RL} &= D_z(s) D_z(xs) g_R^{(e)} g_L^{(f)}, & F_{RR} &= D_z(s) D_z(xs) g_R^{(e)} g_R^{(f)} \end{aligned} \quad (9)$$

are the helicity amplitudes for corresponding processes. Lets calculate first the square of the amplitude for the process $e_L^- + e_R^+ \Rightarrow H + f_L + \bar{f}_R$:

$$\begin{aligned} M(e_L^- e_R^+ \Rightarrow H f_L \bar{f}_R) &= \frac{e^2}{4} \cdot \frac{e M_Z}{2 \sin \theta_W \cdot \cos \theta_W} \times \\ &\times F_{LL} [\bar{v}(p_2, \lambda_2 = 1) \gamma_\mu (1 + \gamma_5) u(p_1, \lambda_1 = -1)] [\bar{u}(q_1, h_1 = 1) \gamma_\mu (1 + \gamma_5) v(q_2, h_2 = 1)]. \end{aligned}$$

Its hermitical conjugate is:

$$\begin{aligned} M^+(e_L^- e_R^+ \Rightarrow H f_L \bar{f}_R) &= \frac{e^2}{4} \cdot \frac{e M_Z}{2 \sin \theta_W \cdot \cos \theta_W} \times \\ &\times F_{LL}^* [\bar{u}(p_1, \lambda_1 = -1) \gamma_\nu (1 + \gamma_5) v(p_2, \lambda_2 = 1)] [\bar{v}(q_2, h_2 = 1) \gamma_\nu (1 + \gamma_5) u(q_1, h_1 = -1)]. \end{aligned}$$

Thus, the squared transition amplitude of this process is given by:

$$|M(e_L^- e_R^+ \Rightarrow H f_L \bar{f}_R)|^2 = \left(\frac{e}{2} \right)^4 \cdot \left(\frac{e M_Z}{2 \sin \theta_W \cdot \cos \theta_W} \right)^2 |F_{LL}|^2 \cdot T_{\mu\nu}^{(1)} \cdot T_{\mu\nu}^{(2)}. \quad (10)$$

Here $T_{\mu\nu}^{(1)}$ and $T_{\mu\nu}^{(2)}$ are the tensors of initial $e^- e^+$ -pairs and final $\bar{f}\bar{f}$ -pairs:

$$\begin{aligned} T_{\mu\nu}^{(1)} &= \text{tr}[\bar{v}(p_2, \lambda_2 = 1) \bar{v}(p_2, \lambda_2 = 1) \gamma_\mu (1 + \gamma_5) \times \\ &\times u(p_1, \lambda_1 = -1) \bar{u}(p_1, \lambda_1 = -1) \gamma_\nu (1 + \gamma_5)] = \\ &= \text{tr} \left[\frac{1}{2} (1 + \gamma_5) \hat{p}_2 \gamma_\mu (1 + \gamma_5) \cdot \frac{1}{2} (1 + \gamma_5) \hat{p}_1 \gamma_\nu (1 + \gamma_5) \right] = \\ &= 8[p_{1\mu} p_{2\nu} + p_{2\mu} p_{1\nu} - (p_1 \cdot p_2) g_{\mu\nu} - i \epsilon_{\mu\nu\rho\sigma} p_{1\rho} p_{2\sigma}]; \end{aligned} \quad (11)$$

$$\begin{aligned} T_{\mu\nu}^{(2)} &= \text{tr}[u(q_1, h_1 = -1) \bar{u}(q_1, h_1 = -1) \gamma_\mu (1 + \gamma_5) \times \\ &\times v(q_2, h_2 = 1) \bar{v}(q_2, h_2 = 1) \gamma_\nu (1 + \gamma_5)] = \\ &= \text{tr} \left[\frac{1}{2} (1 + \gamma_5) \hat{q}_1 \gamma_\mu (1 + \gamma_5) \cdot \frac{1}{2} (1 + \gamma_5) \hat{q}_2 \gamma_\nu (1 + \gamma_5) \right] = \\ &= 8[q_{1\mu} q_{2\nu} + q_{2\mu} q_{1\nu} - (q_1 \cdot q_2) g_{\mu\nu} + i \epsilon_{\mu\nu\alpha\beta} p_{1\alpha} p_{2\beta}]. \end{aligned} \quad (12)$$

For left-handed electrons and right-handed positrons the following relations are fulfilled [1]:

$$u(p_1, \lambda_1 = -1) \bar{u}(p_1, \lambda_1 = -1) = \frac{1}{2} (1 + \gamma_5) \hat{p}_1 ,$$

$$v(p_2, \lambda_2 = 1) \bar{v}(p_2, \lambda_2 = 1) = \frac{1}{2} (1 + \gamma_5) \hat{p}_2$$

The product of tensors of initial and final particles is equal to a simple relation:

$$T_{\mu\nu}^{(1)} \cdot T_{\mu\nu}^{(2)} = 2^8 (p_1 \cdot q_2)(p_2 \cdot q_1). \quad (13)$$

2. Invariant integration method:

Writing the scalar product of 4-momentum in the following form

$$(p_1 \cdot q_2)(p_2 \cdot q_1) = p_{2\mu} p_{1\nu} \cdot q_{1\mu} q_{2\nu}$$

we integrate over momentum of fermion-antifermion pair by invariant methods:
:

$$I_{\mu\nu} = \int q_{1\mu} q_{2\nu} \frac{d\vec{q}_1}{E_1} \cdot \frac{d\vec{q}_2}{E_2} \delta(q_1 + q_2 - q). \quad (14)$$

The result of integration is just a tensor which depends on q_μ vectors

$$I_{\mu\nu} = A q^2 g_{\mu\nu} + B q_\mu q_\nu, \quad (15)$$

A And B are scalar functions. To calculate them we multiply both side of eq. (15) with $g_{\mu\nu}$ and $q_\mu q_\nu$ tensors:

$$g_{\mu\nu} I_{\mu\nu} = 4Aq^2 + Bq^2, \quad q_\mu q_\nu I_{\mu\nu} = Aq^4 + Bq^4. \quad (16)$$

On the other hand we can integrate the relation (14)

$$g_{\mu\nu} I_{\mu\nu} = \frac{1}{2} q^2 \cdot I, \quad q_\mu q_\nu I_{\mu\nu} = \frac{1}{4} q^4 \cdot I. \quad (17)$$

Here the integral

$$I = \int \frac{d\vec{q}_1}{E_1} \cdot \frac{d\vec{q}_2}{E_2} \delta(q_1 + q_2 - q),$$

could be easily calculated in the center of mass frame of fermion-antifermion pair

$$I = 2\pi.$$

To calculate the function A and B we get the following system of equation:

$$\frac{1}{2} q^2 \cdot 2\pi = 4Aq^2 + Bq^2, \quad \frac{1}{4} q^4 \cdot 2\pi = Aq^4 + Bq^4.$$

Here we get $A = \frac{\pi}{6}$ and $B = \frac{\pi}{3}$. So the tensor $I_{\mu\nu}$ will be equal to:

$$I_{\mu\nu} = \frac{\pi}{6} (q^2 g_{\mu\nu} + 2q_\mu q_\nu). \quad (18)$$

In the center of mass frame we get the following expression for $p_{2\mu} p_{1\nu}$ and $I_{\mu\nu}$ tensors product:

$$p_{2\mu} p_{1\nu} \frac{\pi}{6} (q^2 g_{\mu\nu} + 2q_\mu q_\nu) = \frac{\pi}{12} s^2 f(\omega, \theta).$$

where

$$f(\omega, \theta) = 2 \left(1 - \frac{2\omega}{\sqrt{s}} + \frac{M_H^2}{s} \right) + \frac{1}{s} (\omega^2 - M_H^2) \sin^2 \theta, \quad (19)$$

and θ is the angle between momentum of Higgs boson and electron. In the center of mass frame, the cross section for

the process $e_L^- + e_R^+ \Rightarrow H + f_L + \bar{f}_R$ is equal to

$$d\hat{\sigma}(e_L^- e_R^+ \Rightarrow H f_L \bar{f}_R) = \frac{\alpha^3 M_Z^2}{24\pi x_w(1-x_w)} \cdot N_C \cdot s |F_{LL}|^2 f(\omega, \theta) \sqrt{\omega^2 - M_H^2} d\omega d\Omega. \quad (20)$$

Here N_C is the color constant ($N_C = 1$ when the $\mu^- \mu^+$ - and $\tau^- \tau^+$ -pairs are produced and $N_C = 3$ for the case of production of the quark-antiquark pairs) and $x_w = \sin^2 \theta_w$ is the Weinberg parameter.

Analogically we can calculate the cross section for other helicity processes:

$$\begin{aligned} d\sigma(e_L^- e_R^+ \Rightarrow H f_R \bar{f}_L) &= \frac{\alpha^3 M_Z^2}{24\pi x_w(1-x_w)} N_C \cdot s |F_{LR}|^2 f(\omega, \theta) \sqrt{\omega^2 - M_H^2} d\omega d\Omega, \\ d\sigma(e_R^- e_L^+ \Rightarrow H f_L \bar{f}_R) &= \frac{\alpha^3 M_Z^2}{24\pi x_w(1-x_w)} N_C \cdot s |F_{RL}|^2 f(\omega, \theta) \sqrt{\omega^2 - M_H^2} d\omega d\Omega, \\ d\sigma(e_R^- e_L^+ \Rightarrow H f_R \bar{f}_L) &= \frac{\alpha^3 M_Z^2}{24\pi x_w(1-x_w)} N_C \cdot |F_{RR}|^2 f(\omega, \theta) \sqrt{\omega^2 - M_H^2} d\omega d\Omega. \end{aligned} \quad (21)$$

Only by considering the helicity of fermion the differential cross section will be equal to:

$$\begin{aligned} d\sigma(h_1) &= \frac{\alpha^3 M_Z^2}{48\pi x_w(1-x_w)} N_C \cdot s \cdot f(\omega, \theta) \sqrt{\omega^2 - M_H^2} d\omega d\Omega \times \\ &\quad \times [(1+h_1)(|F_{LR}|^2 + |F_{RR}|^2) + (1-h_1)(|F_{LL}|^2 + |F_{RL}|^2)]. \end{aligned} \quad (22)$$

We clearly see from this that the fermion will be longitudinally polarized by way of weak current. The degree of longitudinal polarization for fermion can be calculated by the following expression:

$$P = \frac{d\sigma(h_1 = 1) - d\sigma(h_1 = -1)}{d\sigma(h_1 = 1) + d\sigma(h_1 = -1)} = \frac{|F_{LR}|^2 + |F_{RR}|^2 - |F_{LL}|^2 + |F_{RL}|^2}{|F_{LR}|^2 + |F_{RR}|^2 + |F_{LL}|^2 + |F_{RL}|^2}. \quad (23)$$

By writing the helicity amplitudes we get:

$$P = \frac{(g_R^{(f)})^2 - (g_L^{(f)})^2}{(g_R^{(f)})^2 + (g_L^{(f)})^2}. \quad (24)$$

That is, the degree of longitudinal polarization depends only on fermion coupling constants with Z^0 -boson. By considering the value of Weinberg's parameter $x_w = \sin^2 \theta_w = 0.232$, the degree of longitudinal polarization for lepton pair ($\mu^- \mu^+$ or $\tau^- \tau^+$) is -14% while for quark pairs $u\bar{u}$ or $c\bar{c}$ is -67% and finally for $d\bar{d}$, $s\bar{s}$ or $b\bar{b}$ pairs it will be -90% .

When electron-positron pairs are polarized longitudinally (the summation is carried over fermion-antifermion spin-parities) the differential cross section will be written by the following form:

$$\begin{aligned} d\sigma(\lambda_1, \lambda_2) &= \frac{\alpha^3 M_Z^2}{24\pi x_w(1-x_w)} N_C \cdot s \cdot f(\omega, \theta) \sqrt{\omega^2 - M_H^2} d\omega d\Omega \times \\ &\quad \times \{(1-\lambda_1)(1+\lambda_2)[|F_{LL}|^2 + |F_{RL}|^2] + (1+\lambda_1)(1-\lambda_2)[|F_{RR}|^2 + |F_{RL}|^2]\}. \end{aligned} \quad (25)$$

It should be noted that for arbitrary polarized electron-positron pairs the process $e^- + e^+ \Rightarrow H + f + \bar{f}$ is worked by N.Guliyev, I.Jafarov and others [7]. The result that we get for annihilation of longitudinal electron-positron pairs coincides with the result of this work.

As we see from the equation (25) the cross section we get for $e_L^- + e_R^+ \Rightarrow H + f + \bar{f}$ is different than what we get for $e_R^- + e_L^+ \Rightarrow H + f + \bar{f}$ i. e. The left-right spin asymmetry should be observed:

$$A_{LR} = \frac{d\sigma(e_L^- e_R^+ \Rightarrow H\bar{f}\bar{f}) - d\sigma(e_R^- e_L^+ \Rightarrow H\bar{f}\bar{f})}{d\sigma(e_L^- e_R^+ \Rightarrow H\bar{f}\bar{f}) + d\sigma(e_R^- e_L^+ \Rightarrow H\bar{f}\bar{f})} = \frac{|F_{LL}|^2 + |F_{LR}|^2 - |F_{RR}|^2 - |F_{RL}|^2}{|F_{LL}|^2 + |F_{LR}|^2 + |F_{RR}|^2 + |F_{RL}|^2}. \quad (26)$$

The left-right spin asymmetry depends only on coupling constants of electron with Z^0 -boson:

$$A_{LR} = \frac{(g_L^{(e)})^2 - (g_R^{(e)})^2}{(g_L^{(e)})^2 + (g_R^{(e)})^2} = \frac{\frac{1}{4} - x_w}{\frac{1}{4} - x_w + 2x_w^2}, \quad (27)$$

And this asymmetry take the value $A_{LR} = 14\%$ when $x_w = 0.232$.

The distributions of Higgs boson over angles and energy are calculated and given as follow for the unpolarized particles:

$$\begin{aligned} \frac{d\sigma}{d\omega d\Omega} &= \frac{\alpha^3 M_Z^2 N_C}{24\pi x_w (1-x_w)} s \cdot [|F_{LL}|^2 + |F_{RL}|^2 + |F_{RL}|^2 + |F_{RR}|^2] \times \\ &\times \sqrt{\omega^2 - M_H^2} d\omega d\Omega \left[2 \left(1 - \frac{2\omega}{\sqrt{s}} + \frac{M_H^2}{s} \right) + \frac{1}{s} (\omega^2 - M_H^2) \sin^2 \theta \right], \end{aligned} \quad (28)$$

$$\begin{aligned} \frac{d\sigma}{d\omega} &= \frac{\alpha^3 M_Z^2 N_C}{3x_w (1-x_w)} [|F_{LL}|^2 + |F_{LR}|^2 + |F_{RL}|^2 + |F_{RR}|^2] \times \\ &\times \left[s - 2\sqrt{s}\omega + \frac{1}{3} (\omega^2 + 2M_H^2) \right] \sqrt{\omega^2 - M_H^2}. \end{aligned} \quad (29)$$

The distribution of Higgs boson over angles is depicted in Fig.2 for the processes $e^- + e^+ \Rightarrow H + u + \bar{u}$, $e^- + e^+ \Rightarrow H + d + \bar{d}$ at the energy $\sqrt{s} = 500 \text{ GeV}$, Weinberg parameter $x_w = 0.232$, $M_H = 125 \text{ GeV}$ and $\omega = 257.8 \text{ GeV}$.

As we can see from the Fig. 2, as the angle of outgoing Higgs boson increase, the cross section also increase and reaches to its maximum at the value of $\theta = 90^\circ$. By further increase of angle the cross section starts to decrease.

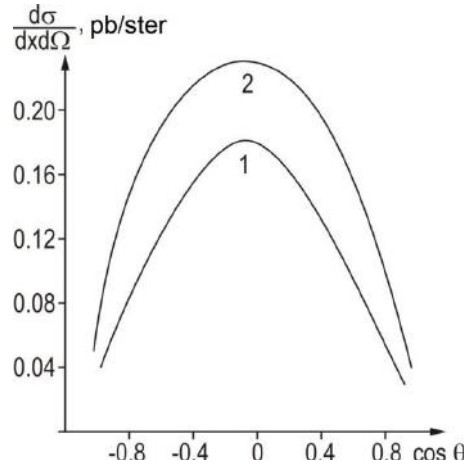


Fig. 2. The cross section $\frac{d\sigma}{dxd\Omega}$ for the reactions $e^- + e^+ \Rightarrow H + u + \bar{u}$, $e^- + e^+ \Rightarrow H + d + \bar{d}$ As a function of $\cos \theta$ (1 and 2 lines)

In Fig. 3 we plot the cross section for the processes $e^- + e^+ \Rightarrow H + u + \bar{u}$, $e^- + e^+ \Rightarrow H + d + \bar{d}$ as function

of M_H at $xs = M_z^2$, $\sqrt{s} = 500 \text{ GeV}$, $x_w = 0.232$. As we can see, as the mass of Higgs boson increase the cross section decrease.

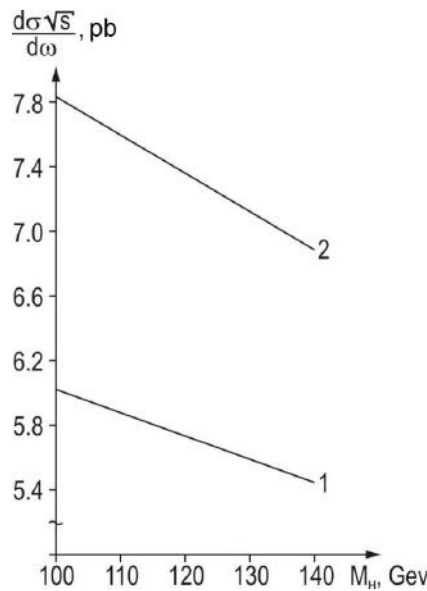


Fig. 3. The cross section $\frac{d\sigma}{dx d\Omega}$ for the processes $e^- + e^+ \Rightarrow H + u + \bar{u}$, $e^- + e^+ \Rightarrow H + d + \bar{d}$ As a function of M_H (the lines 1 and 2)

CONCLUSION

The cross section we get for $e_L^- + e_R^+ \Rightarrow H + f + \bar{f}$ is different than what we get for $e_R^- + e_L^+ \Rightarrow H + f + \bar{f}$ i.e. the left-right spin asymmetry should be observed.

As the angle of outgoing Higgs boson increase, the

cross section also increases and reaches to its maximum at the value of $\theta = 90^\circ$. By further increase of angle the cross section starts to decrease.

By increasing the Higgs boson the cross section will be decreased.

- [1] S.Q. Abdullayev Lepton-lepton və lepton-hadron qarşılıqlı təsirlərində zəif cərəyan effektləri (I hissə), Bakı, 2012, «AM 965 MMC» nəşr., 482 səh.
- [2] S.Q. Abdullayev. Lepton-lepton və lepton-hadron qarşılıqlı təsirlərində zəif cərəyan effektləri (II hissə), Bakı, 2013, «AM 965 MMC» nəşr., 304 səh.
- [3] CDF Collaboration. Combined search for the Standard Model Higgs boson decaying to a $b\bar{b}$ pair using the full CDF data set. arxiv:1207.1707.
- [4] ATLAS Collaboration. Observation of a new particle

- in the search for the Standard Model Higgs boson with the ATLAS detector at the LHC. Phys. Lett., 2012, B 716, p. 1-29.
- [5] CMS Collaboration. Observation of a new boson at a mass of 125 GeV with the CMS experiment at the LHC. arxiv: 1207.7235.
- [6] V.A. Rubakov. Uspekhi fizicheskikh nauk. 2012, t. 182, n. 10, s. 1017-1025. (in Russian)
- [7] N.A. Gulyiyev, I.G. Jafarov i dr. Yadernaya fizika, 1984, t.40, vip. 1(7), s. 174-180. (in Russian)

Received: 08.04.2014

**THE TEMPERATURE DEPENDENT ELECTRICAL CHARACTERISTICS
OF Au/TiO₂/n-Si METAL-INSULATOR-SEMICONDUCTOR STRUCTURES
USİNG C-V AND G/w-V MEASUREMENTS**

**MURAT SEL^a, AHMET ASİMOV^b, ELCHİN HUSEYNOV^c,
MATLAB MIRZAYEV^c, AZAR SADIGOV^{c,d}**

^a*Physics Department, Faculty of Arts and Sciences, Gazi University, Teknikokullar, 06500 Ankara,
TURKEY*

^b*Department of Physics, Faculty of Sciences and Arts, Uludag University, 16059 Gorukle, Bursa,
TURKEY*

^c*The Institute of Radiation Problems of ANAS, AZ1143, B. Vakhabzadeh 9, Baku, AZERBAIJAN*

^d*Zecotek Photonics Inc. Unit 1120 - 21331 Gordon Way Richmond, BC, V6W 1J9, CANADA*

Corresponding author. Tel.: 00905350628201

E-mail address: fizikasimov@hotmail.com, hus.elchin@gmail.com, elchin55@yahoo.com

The temperature dependence of capacitance–voltage (C – V) and the conductance–voltage (G / w – V) characteristics of Au/TiO₂/n-Si Metal–Insulator–Semiconductor Schottky diode were investigated by considering the effect of series resistance (R_s) and interface states N_{ss} in a wide temperature range (160–380 K). Using I/C^2 - V graphic data; diffusion voltage V_D , barrier height Φ_B , N_D donor concentration, width of depletion layer have been calculated. At room temperature barrier height value has been calculated as 0.86 eV from C – V measurements.

Keywords: Schottky barrier diode; Ideality factor; Interface states; insulator layer; Series resistance.

PACS: 81.05.Cy, 81.05.Hd, ACS: 81.05.Cv; 52.77.Dq

1. INTRODUCTION

The Metal–Semiconductor (MS) structures have important applications in bipolar integrated circuits such as microwave detectors, varactors and field-effect transistors. Electrical characteristics of Metal–Insulator–Semiconductor (MIS) structures are influenced by various non-idealities such as formation of and insulator layer and the energy distribution profile of interface states at the metal/semiconductor interface, series resistance and inhomogeneous Schottky barrier heights [1-7]. The titanium dioxide (TiO₂) thin films are extensively studied due to their interesting chemical, optical and electrical properties. Various methods have been employed to prepare TiO₂ thin films, among which are e-beam evaporation [6], sol–gel process *C* and chemical vapor deposition [8-10] Experimental results, especially only at room temperature, does not give detailed information about the conduction mechanisms or the nature of the barrier formation at the MS or MIS Schottky diodes. Therefore, the C – V and G / w – V characteristics of these devices have been studied in the wide temperature range (160–380 K). In this study, the C – V – T and G / w – V – T characteristics of metal-semiconductor (Al/p-Si) Schottky diodes with the thermal growth interfacial layer were investigated by considering series resistance effect in the wide temperature range (160–380K). In addition, we investigated the effects of donor concentration N_D and series resistance (R_s) on the C – V and G / w – V characteristics.

2. EXPERIMENTAL PROCEDURE

The Au/TiO₂/n-Si MIS structure was fabricated on a quarter of 2 in diameter float zone (100) n-type (S doped) single crystal silicon (Si) wafer having thickness of 380 μ m. The sample was ultrasonically cleaned in

trichlorethylene and ethanol, etched by H₂SO₄/H₂O₂/H₂O=5:1:1 (weight ratio) solution for 30 s., rinsed by propylene glycol and blown with dry nitrogen gas. The high purity gold with a thickness of 1750Å was thermally evaporated from tungsten filament onto the whole back side on the n-Si wafer at a pressure of 1×10^{-6} Torr in liquid nitrogen trapped oil-free ultra high vacuum pump system. Preceding each cleaning step, the wafer was rinsed thoroughly in de-ionized water of resistivity of 18 MΩ cm. The ohmic contact was formed by sintering the evaporated Au back contact at 350°C for 5 min in a flowing dry oxygen ambient at rate of 1 lt/min. After oxidation, circular dots of 1mm diameter and 1800Å thick gold contacts were deposited onto the oxidized surface of the wafer through a metal shadow mask in a liquid nitrogen trapped vacuum system in a vacuum of 1×10^{-6} Torr.

The capacitance–voltage (C – V) and conductance–voltage (G / w – V) characteristics of Au/TiO₂/n-Si Schottky (SDs) were measured in the temperature range of 160–380K. The C – V and G / w – V measurements were carried out at 1 MHz by using an HP4192 A LF impedance analyzer.

3. RESULTS AND DISCUSSION

The capacitance–voltage (C – V) and conductance–voltage (G / w – V) characteristics of the Au/TiO₂/n-Si (MIS) structure were measured in the temperature range (160–380) K and are given in Fig.1. In Schottky diodes, the depletion layer capacitance can be expressed as [1,2]. As seen in Fig.1 the measured C and G / w are strongly dependent on bias voltage and temperature. As shown in Fig. 1, the values of C increase systematically with increasing temperature.

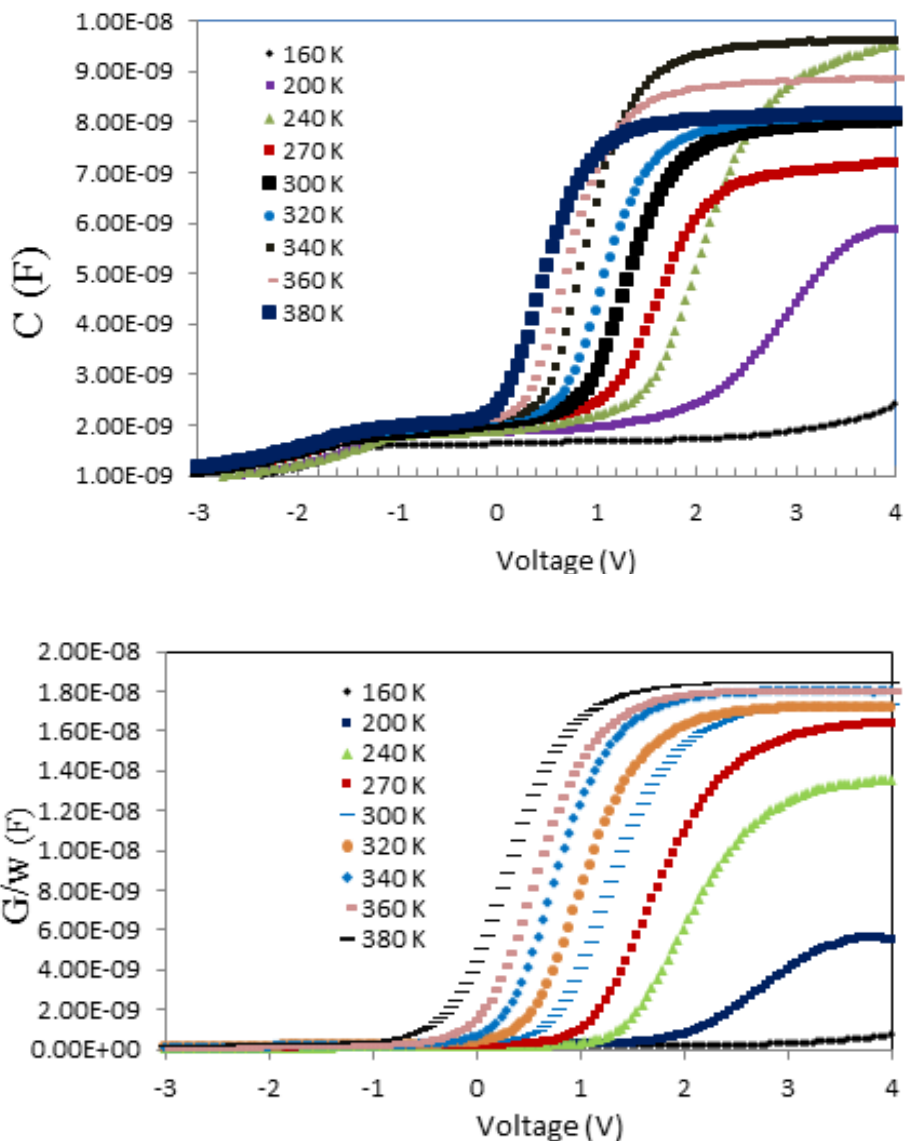


Fig. 1. The temperature dependent plots of (a) the capacitance–voltage and (b) conductance–voltage characteristics of Au/TiO₂/n-Si (MIS) structure in the range (160-380) K.

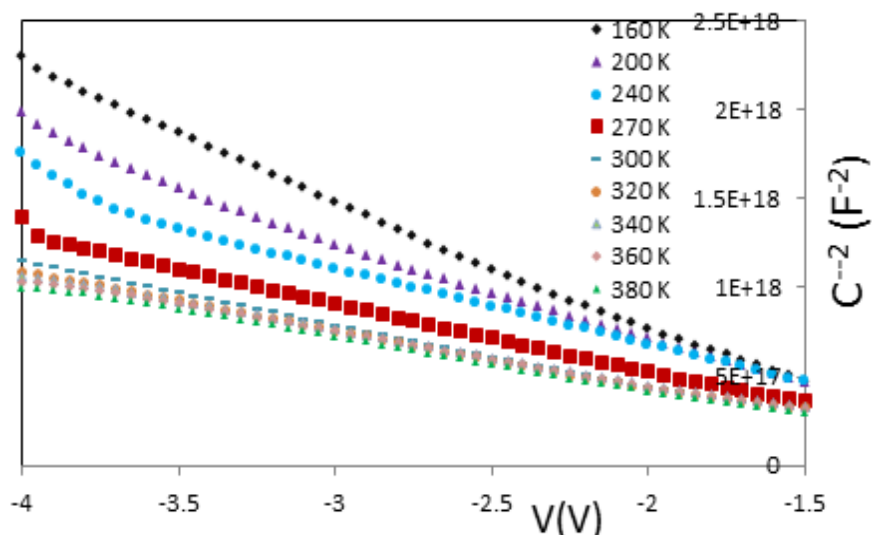


Fig. 2. C^2 – V characteristics for the Au/TiO₂/n-Si structure in the range (160-380) K.

The peak positions shift towards higher positive voltages with increasing temperature, and the peak value of the capacitance has a maximum at 380K. Such behavior of C and G/w is attributed to the particular distribution of interface states at Si/TiO₂ interfaces and R_s of the structure [1-5]. At low frequencies, the can easily follow the ac signal and yield an excess capacitance, which depends on the frequency and time constant of interface states. However, in a sufficiently high frequency limit ($f=1000$ kHz), the N_{ss} can hardly follow the ac signal and contribution of the interface states capacitance to the total capacitance may be neglected. R_s is an important parameter which causes deviations in the $C-V$ and $G/w-V$ characteristics of MIS structure and it can be subtracted from the measured capacitance (C_{ma}) and conductance (G_{ma}) in the strong accumulation region at a sufficiently high frequency [11-14].

The depletion layer capacitance in MIS structure can be expressed as,

$$\frac{\partial C^{-2}}{\partial V} = \frac{2}{q\epsilon_s A^2 N_D} \quad (1)$$

or

$$C_2 = \frac{1}{n_{CV}} = \frac{2}{q\epsilon_s N_D \left(\frac{\partial C^2}{\partial V} \right)} \quad (2)$$

Eq. (1), A is the area of the diode, the dielectric constant of the Si (=12 ϵ_0), q is the electronic charge and N_D is the donor concentration. V is the applied reverse bias and V_0 is the intercept of C^2 vs V plot with the voltage axis and is given by

$$V_d = V_0 + \frac{kT}{q} \quad (3)$$

where V_d is the diffusion potential, T is the absolute temperature and k is the Boltzmann constant. The diffusion potential or built-in potential is usually measured by extrapolating I/C^2-V plot to the V -axis. The barrier height, Φ_{bo} , from $C-V$ measurement is defined by

$$\Phi_{bo}(C-V) = V_d + E_F \quad (4)$$

where E_F is the Fermi energy According to Eq. (4), the measured barrier height $\Phi_{bo}(C-V)$ is 0,86 eV and the donor concentration is determined to be $N_d=1.53\times 10^{16}$ cm⁻³ density of states in the conduction band, which is $N_c=2.8\times 10^{19}$ cm⁻³ for Si at room temperature. From the reverse bias $C-V$ measurements, the barrier heights (Φ_b) were calculated at different temperature using the intercept voltage V_o of the C^2-V plots from the Eq. (3) and were given in Table 1. The values of V_o , V_d , N_D , E_F and Φ_b were calculated from C^2-V plot for different temperature, and presented in Table 1.

Table 1.

The values of various parameters for the Au/TiO₂/n-Si (100) Schottky MIS diodes determined from the $C-V$ and $G/w-V$ characteristics in the temperature range of 160–380 K.

T (K)	V_0 (V)	V_d (V)	N_d (cm ⁻³)	E_f (eV)	Φ_B (eV)
160	0.863	0.485	1.31E+16	0.079	0.565
200	0.789	0.502	1.46E+16	0.103	0.605
240	0.659	0.527	1.42E+16	0.129	0.656
270	0.611	0.634	1.59E+16	0.144	0.778
300	0.593	0.637	1.53E+16	0.162	0.863
320	0.426	0.682	1.97E+16	0.175	0.897
340	0.304	0.736	1.97E+16	0.189	0.925
360	0.239	0.765	2.06E+16	0.201	0.966
380	0.134	0.876	2.35E+16	0.211	1.087

Series resistance is the real part of the impedance and can be expressed as

$$R_s = \frac{G_{mak}}{G_{mak}^2 + \omega^2 C_{mak}^2} \quad (5)$$

where C_{ma} and G_{ma} represent the measured capacitance and conductance in the strong accumulation region. The series resistance is an important parameter..

Therefore, voltage dependent values of the series resistance R_s are calculated from Eq. (5). As shown in Fig. 3, the values of R_s increase with increasing temperature.

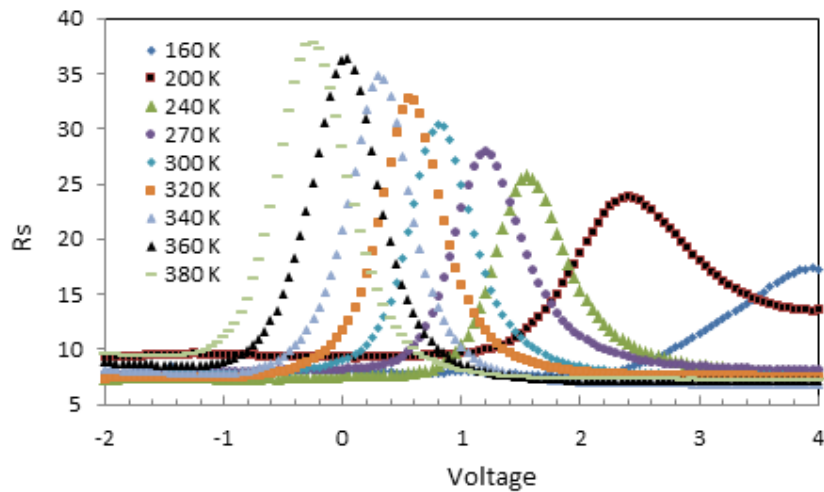


Fig. 3. The variation of the series resistance as a function of bias voltage at different temperatures at 1 MHz.

4. CONCLUSION

The forward and reverse bias capacitance-voltage-temperature ($C-V-T$) and conductance-voltage-temperature ($G/w-V-T$) characteristics of the metal-insulator-semiconductor (Au/TiO₂/n-Si) Schottky diodes (SDs) were measured in the temperature range of 160–380K. The effects of the series resistance and (R_s) and donor concentration N_D of the sample on the $C-V$ characteristics are investigated. The R_s vs. V plot gives a peak for each temperature, decreasing with increasing

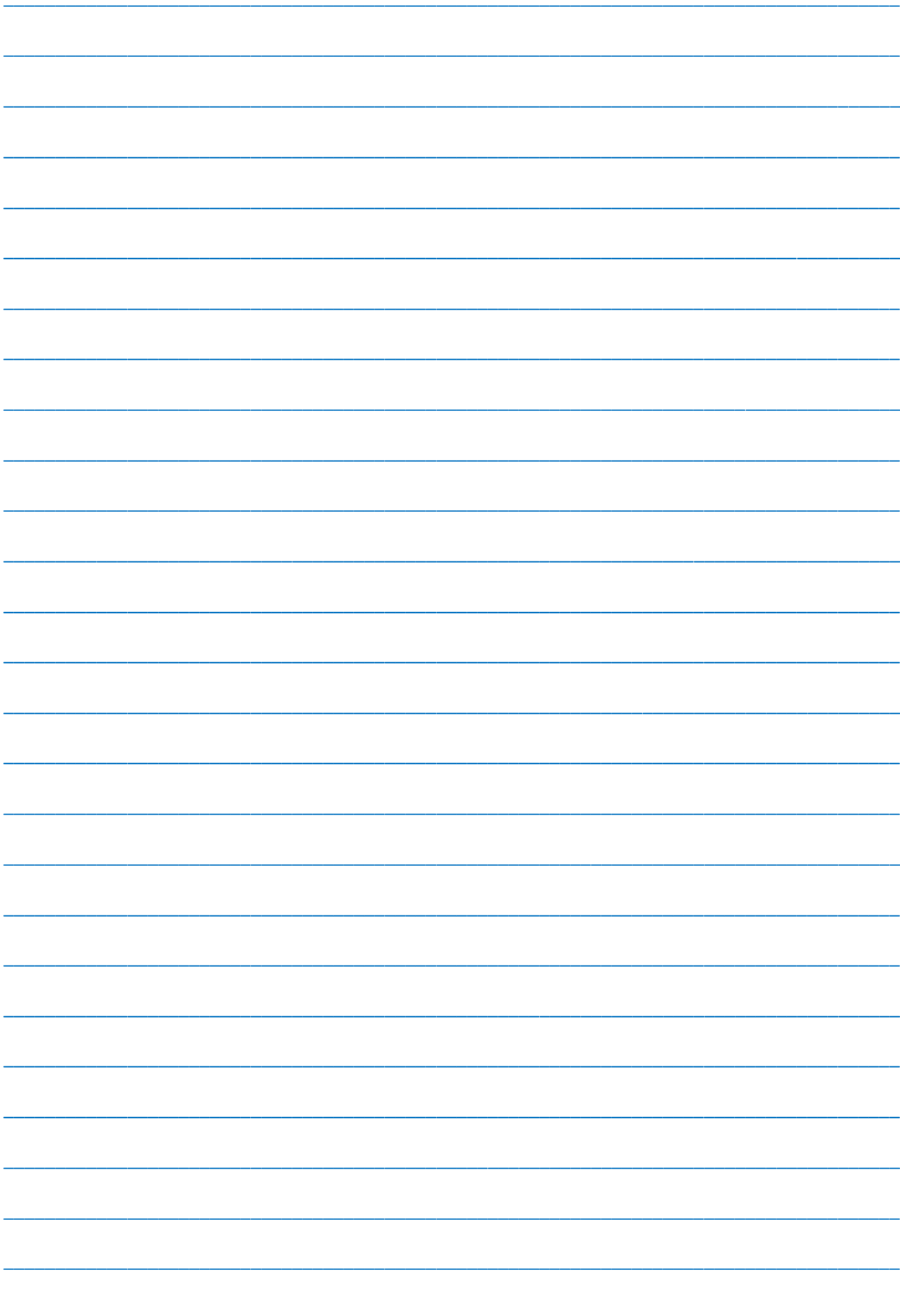
temperature. These results show that the prepared MIS structures are controlled by the interfacial insulator layer and interface states, which are responsible for the non-ideal behavior of $C-V$ and $G/w-V$ characteristics. SBD parameters such as V_0 , V_d , N_D , E_F , Φ_b and the series resistance (R_s) are investigated as functions of temperature. The $C-V$ and ($G/w-V$) characteristics confirm that the, R_s , N_{ss} and thickness of the insulator layer (d) are important parameters that strongly influence the main electric parameters of the MIS Schottky diodes.

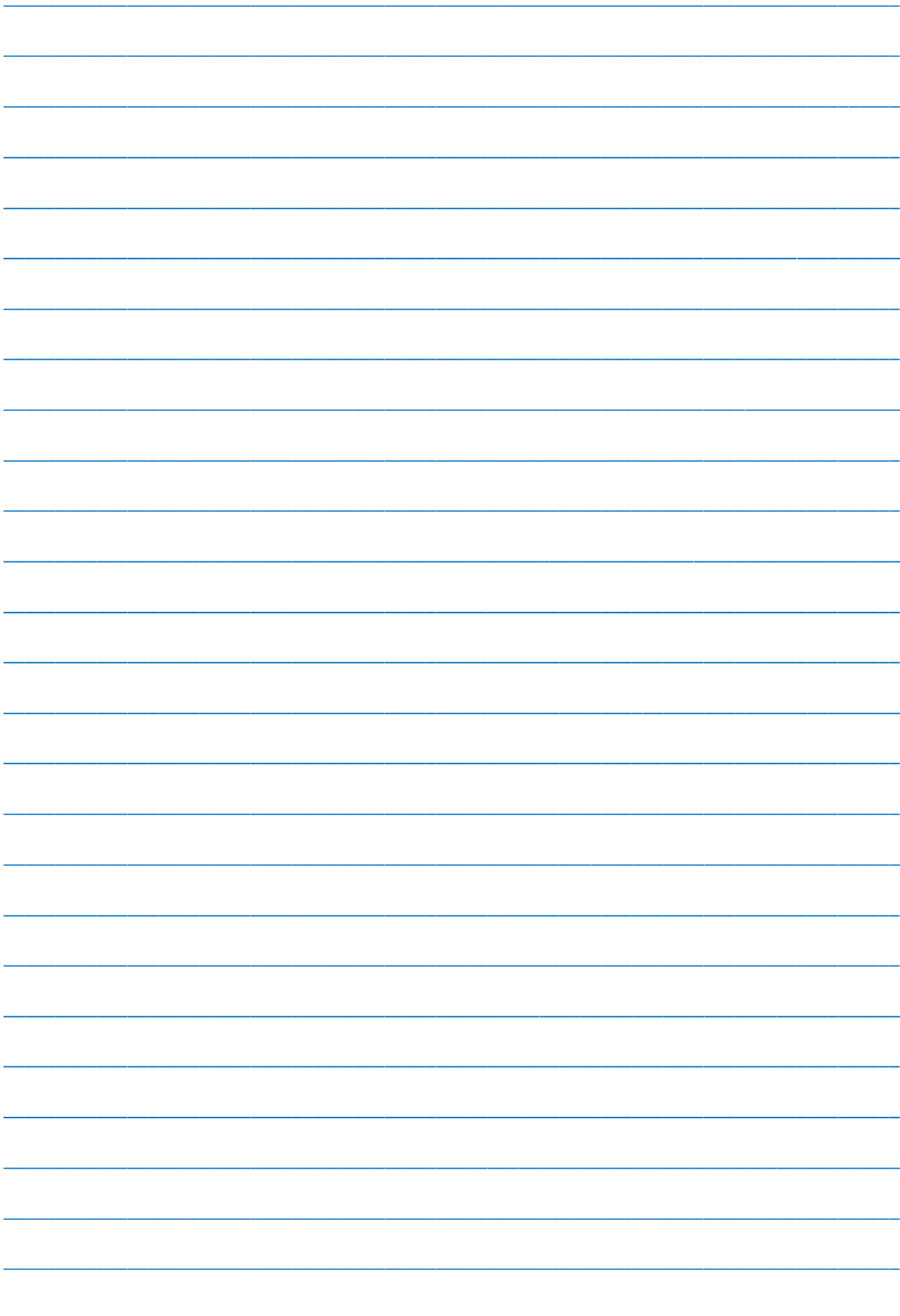
-
- | | |
|---|--|
| [1] E.H. Rhoderick, R.H. Williams. Metal-semiconductor contacts, 2nd ed. Oxford; 1988. | [8] H.Y. Ha, S.W. Nam, T.H. Lim, I.H. Oh, S.A. Hong. J. Membr. Sci. 111 (1996) 81. |
| [2] S.M. Sze. Physics of semiconductor structures. 2nd ed. New York; 1981. | [9] S.K. Cheung, N.W. Cheung. Appl. Phys. Lett. 49 (1986) 85. |
| [3] H.C. Card, E.H. Rhoderick, J. Phys. D4 (1971) 1589. | [10] A. Türüt, M. Sağlam, H. Efeoğlu, N. Yalçın, M. Yıldırım, B. Abay. Physica B 205 (1995) 41. |
| [4] A. Tataroğlu, Ş. Altindal. Microelectron. Eng. 83 (2006) 582. | [11] D.A. Neamen, in: Semiconductors Physics and Devices, R. R. Donnelley & Sons Company, Sydney, 1992 |
| [5] S. Chakraborty, M.K. Bera, P.K. Bose, C.K. Maiti, Semicond.Sci.Technol.21 (2006) 335. | [12] Ş. Karataş, Ş. Altindal, M. Çakar. Physica B, 357-386, (2005). |
| [6] G. Sanon, R. Rup, A. Mansingh. Thin Solid Films 190 (1990) 287. | [13] J.H. Werner, H.H. Guttler. J. Appl. Phys.1991; 69:1522. |
| [7] J.P. Chatelon, C. Terrier, E. Bernstein, R. Berjoan, J.A. Roger. Thin Solid Films 247 (1994) 162. | [14] İ. Dökme, Ş. Altindal. Physica B 391, 59–64 (2007). |

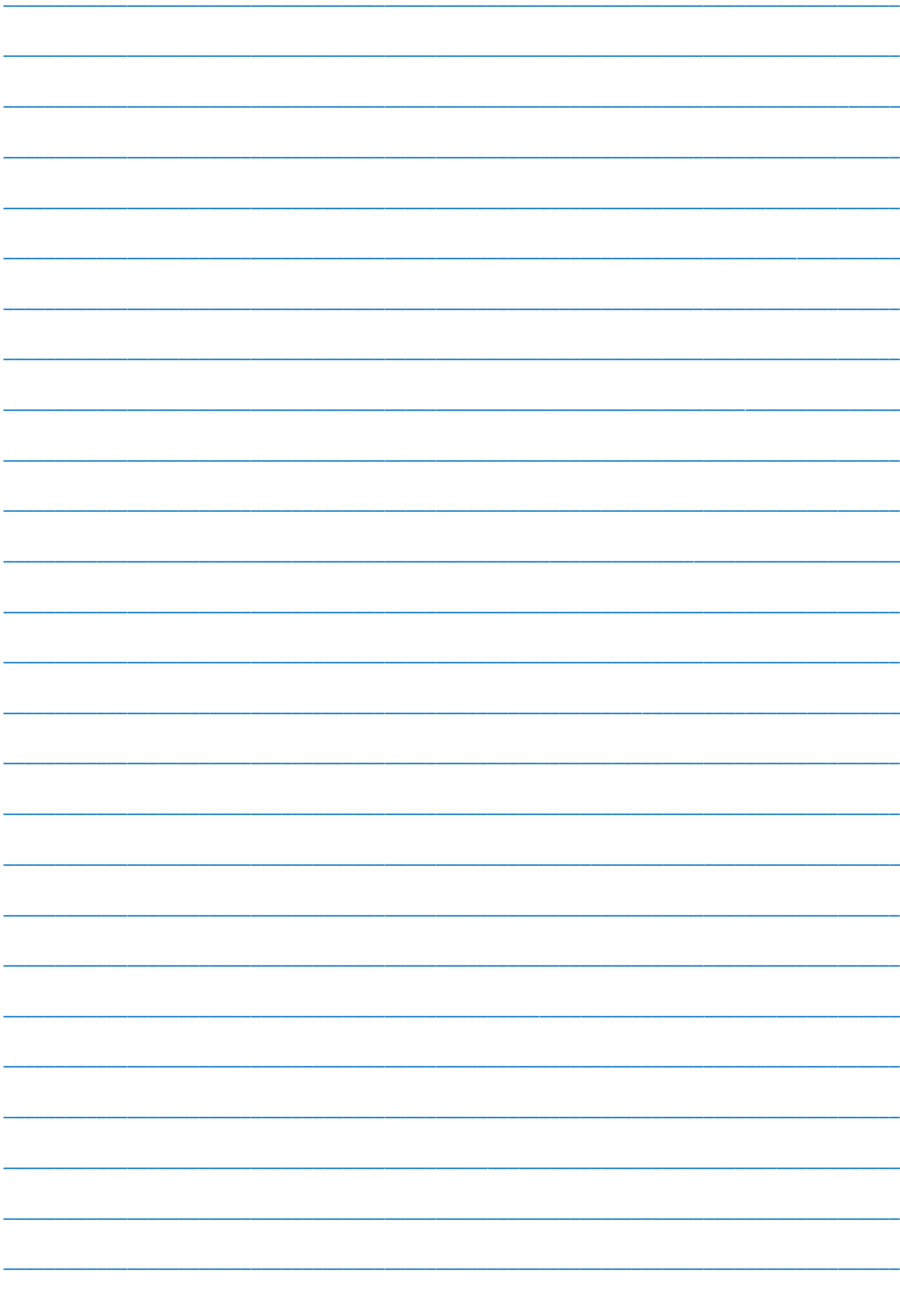
Received: 03.04.2014

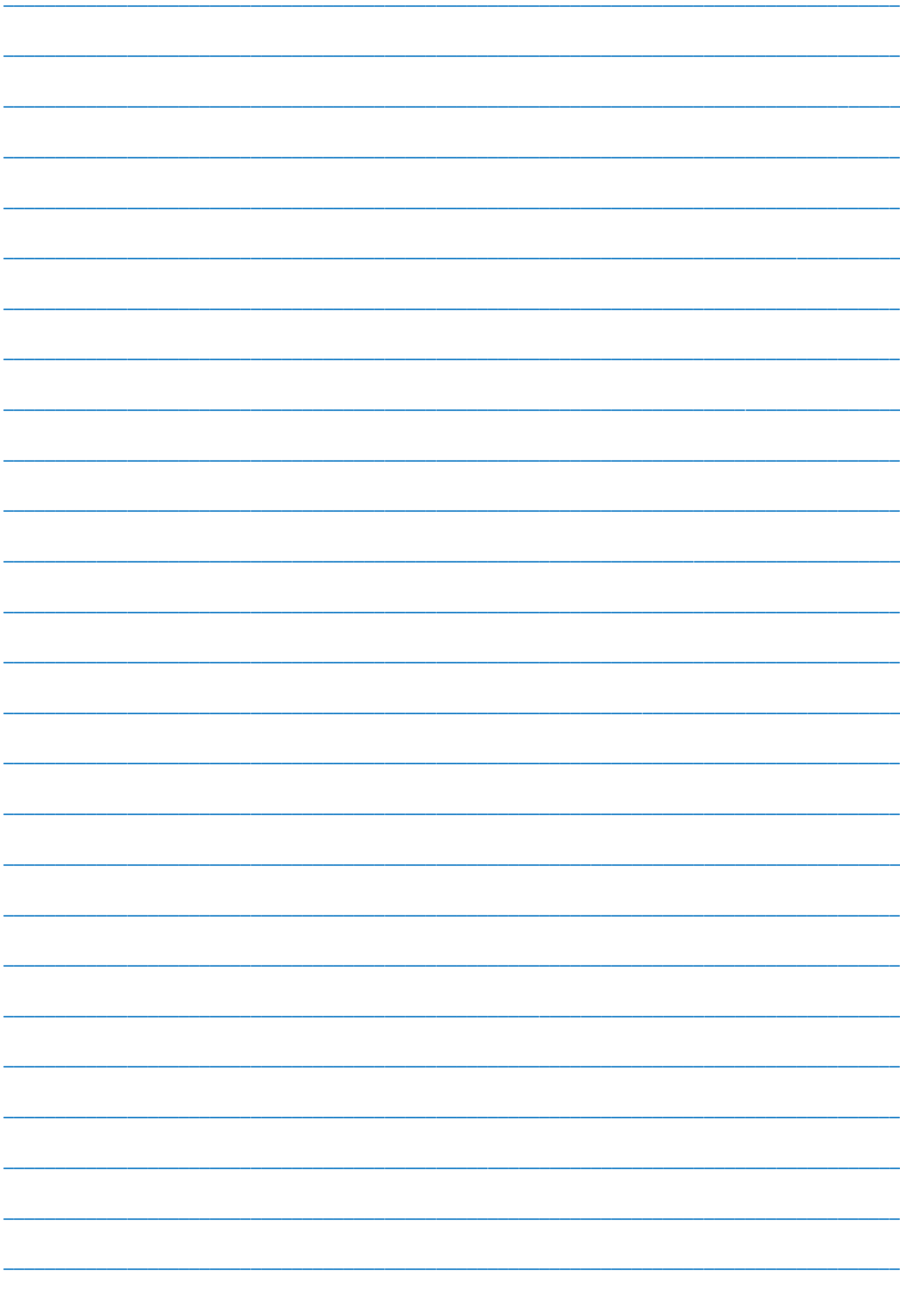
CONTENTS

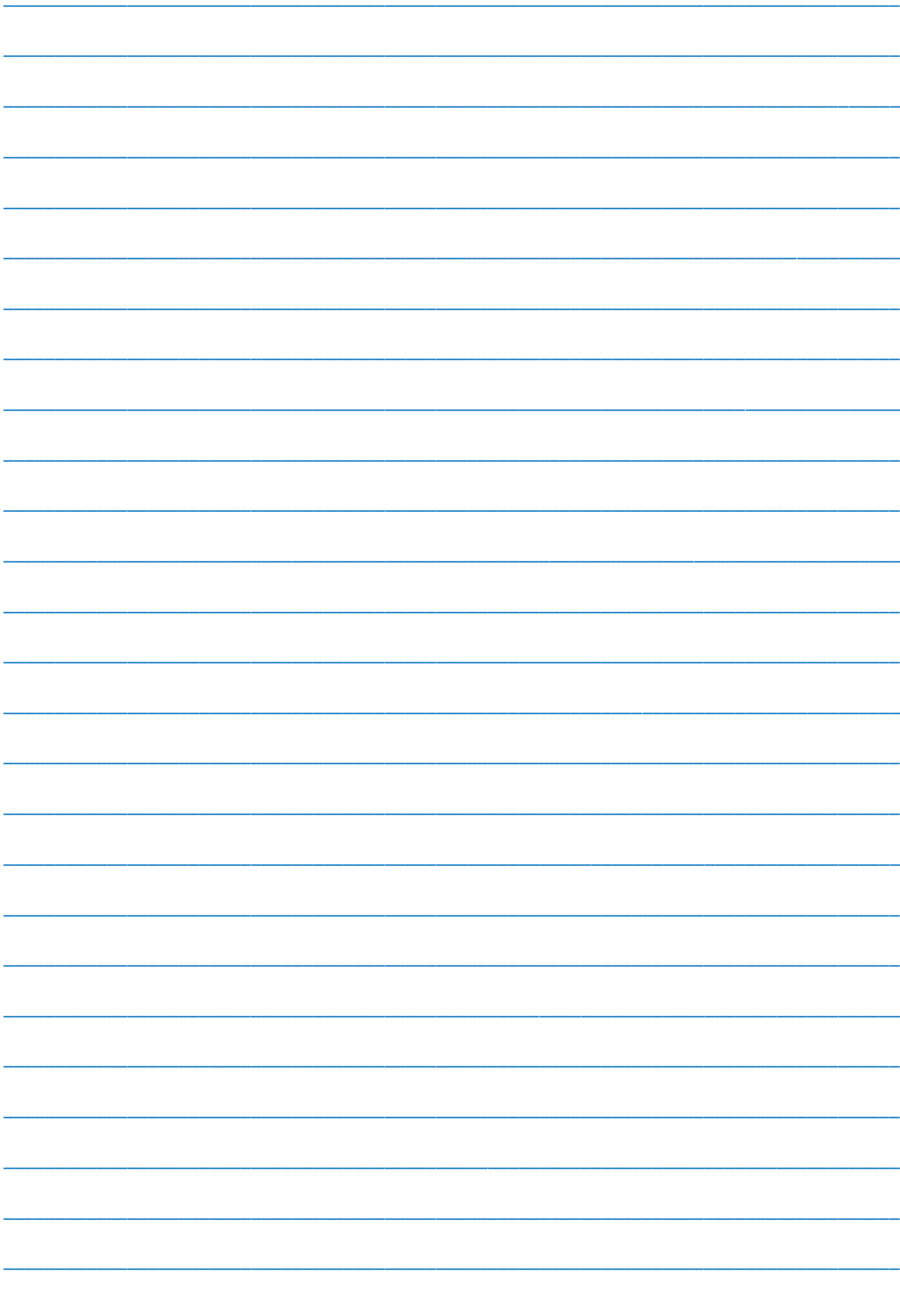
1.	The frequency dependence of micropixel avalanche photodiode capacitance E.A. Jafarova, Z.Y. Sadigov, F.I. Akhmedov, A.Z. Sadigov, L.A. Aliyeva	3
2.	Kinetics of phase transformations in CuIn ₅ Se ₈ thin films A.Ch. Mamedova, N.K. Kerimova, D.I. Ismayilov	6
3.	Thermal expansion, isothermal compression and heat capacity difference at constant pressure (C _P) and constant volume (C _V) in solid solutions (TlGaSe ₂) _{1-x} (TlInS ₂) _x (x = 0.1;0.2) M.M. Kurbanov, M.M. Godjayev, A.M. Akhmedova	9
4.	Energy spectrum and scattering mechanism of charge carriers in monocrystalline alloys Bi _{1-x} Sb _x (0, ≤ x ≤ 0,25) in the temperature range T = 77-300K B.A. Tairov, H.A. Gasanova	12
5.	Evolution equation of Wigner function for relativistic quantum systems Sh.M. Nagiyev, K.Sh. Jafarova	21
6.	Electronic structure and conformational-dynamic properties of allatostatin molecule L.I. Veliyeva, E.Z. Aliyev	25
7.	Higgs boson production in electron-positron annihilation S.Q. Abdullayev, M.Sh. Gojayev, F.A. Saddigh	29
8.	The temperature dependent electrical characteristics of Au/TiO ₂ /n-Si metal-insulator-semiconductor structures using C-V and G/w-V measurements Murat Sel, Ahmet Asimov, Elchin Huseynov, Matlab Mirzayev, Azar Sadigov	36

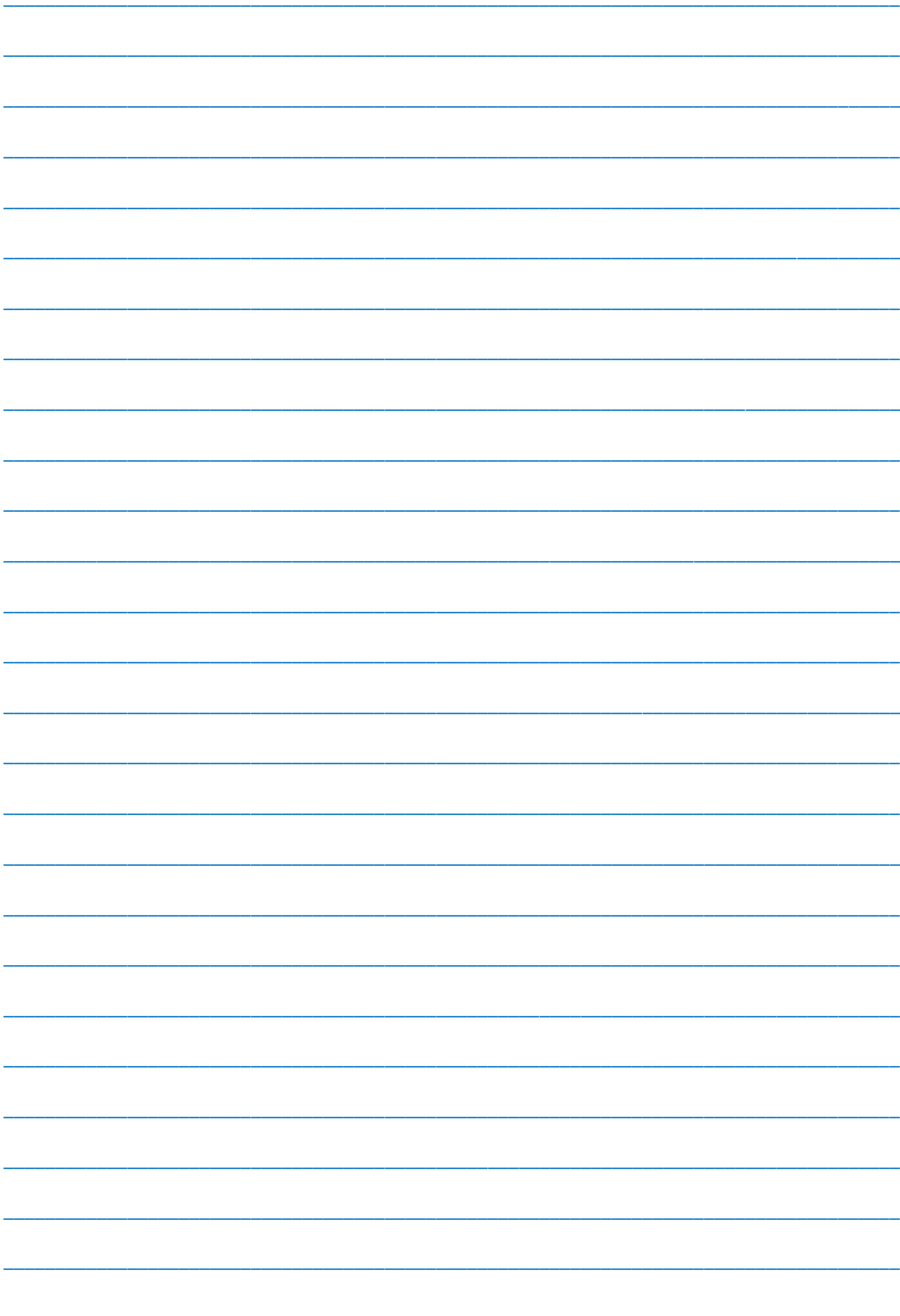


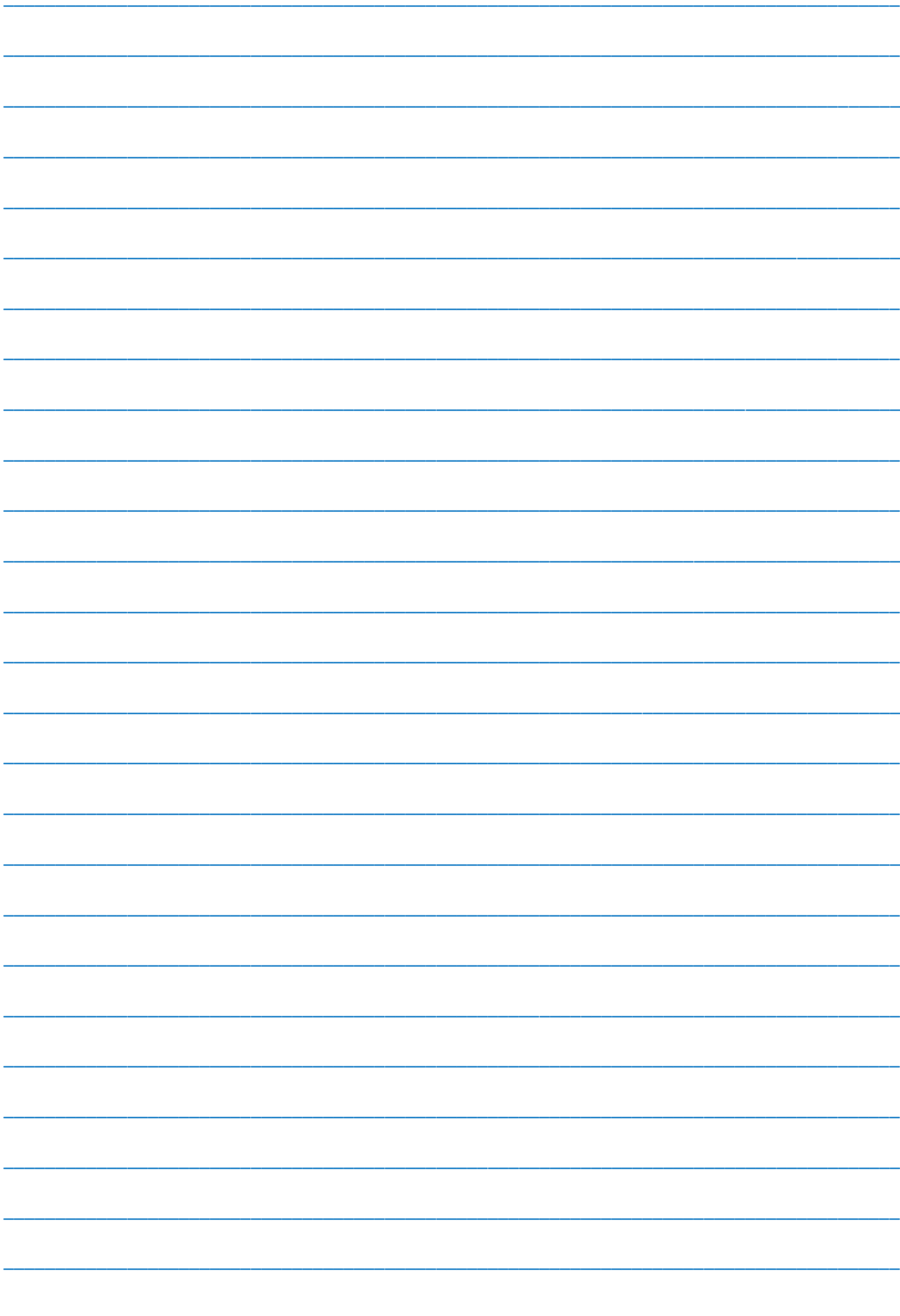














www.physics.gov.az